Mechanical Systems and Signal Processing 184 (2023) 109654

Contents lists available at ScienceDirect

Mechanical Systems and Signal Processing

journal homepage: www.elsevier.com/locate/ymssp

An adaptive-noise Augmented Kalman Filter approach for input-state estimation in structural dynamics

S. Vettori [a,b,*], E. Di Lorenzo [a], B. Peeters [a], M.M. Luczak [c,d], E. Chatzi [b]

[a] Siemens Digital Industries Software, Interleuvenlaan 68, 3001 Leuven, Belgium
[b] Institute of Structural Engineering, ETH Zürich, Stefano-Franscini-Platz 5, 8093 Zürich, Switzerland
[c] Department of Wind Energy, Technical University of Denmark, Frederiksborgvej 399, 4000 Roskilde, Denmark
[d] Faculty of Mechanical Engineering and Ship Technology, Gdańsk University of Technology, Narutowicza 11/12, 80-233 Gdańsk, Poland

ARTICLE INFO

Communicated by J.E. Mottershead

Keywords:
Augmented Kalman Filter
Input-state estimation
Noise statistics
Modal Expansion
Wind turbine blades
Digital Twin

ABSTRACT

The establishment of a Digital Twin of an operating engineered system can increase the potency of Structural Health Monitoring (SHM) tools, which are then bestowed with enhanced predictive capabilities. This is particularly relevant for wind energy infrastructures, where the definition of remaining useful life is a main driver for assessing the efficacy of these systems. In order to ensure a proper representation of the physical structure, the monitored response of the Digital Twin should match the one experienced by the actual system throughout the complete spectrum of its operational conditions. In most typical SHM configurations, it is only possible to rely on output-only measurements, acquired from finite positions within a structure, which naturally raises the challenge of recovering the full-field operational response, including unmeasured locations. This problem, also known as Virtual Sensing (VS), has been treated using different schemes, including Bayesian filtering and Modal Expansion (ME). In this paper, the Augmented Kalman Filter (AKF) is exploited to this end; a tool which allows for simultaneous full-field response and unmeasured input prediction. The common issue of Bayesian filtering relies on calibration of the filters defining parameters, namely the assumed measurement and process noise covariance levels. While the first is directly related to the accuracy of the employed physical sensors, the latter often acts as a tuning parameter for improving the reliability of the prediction. The process noise covariance adjustment is often performed in an offline fashion, either by making use of regularization methods, e.g., the L-curve method, or via trial and error. In this work, we propose a methodology for automated process noise covariance adaptation, relying on response estimates recovered by means of an improved ME approach. The method is validated on experimental data from a large scale research Wind Turbine (WT) blade made of glass fiber reinforced plastics.

1. Introduction

Wind energy infrastructure represents an active area of research on multiple fronts, but particularly within the structural dynamics domain, where multiple challenges arise due to the stochastic nature of the loads these systems are exposed to and the inaccessibility of components after their installation. Digital Twins [1] of Wind Turbine (WT) components [2], i.e., digital representations featuring encoded information on the structure "as-is", can facilitate the monitoring of the performance of these

* Corresponding author at: Siemens Digital Industries Software, Interleuvenlaan 68, 3001 Leuven, Belgium.
E-mail addresses: silvia.vettori@siemens.com (S. Vettori), emilio.dilorenzo@siemens.com (E. Di Lorenzo), bart.peeters@siemens.com (B. Peeters), marlucza@pg.edu.pl (M.M. Luczak), chatzi@ibk.baug.ethz.ch (E. Chatzi).

https://doi.org/10.1016/j.ymssp.2022.109654
Received 20 December 2021; Received in revised form 8 July 2022; Accepted 4 August 2022
Available online 26 August 2022

systems throughout the structural life-cycle. Blades comprise WT components of elevated importance and complexity. Extensive testing is usually performed on blades in order to build a test-validated Digital Twin and to prove that these can withstand the anticipated loads in field conditions [3]. Although more attention is usually placed on static [4,5] and fatigue tests [6–10], dynamic tests are also adopted for identifying basic dynamic properties, essential for the structural integrity of the entire WT. Dynamic tests [11–16] require a vibration source, which could be achieved via use of a shaker or by simple hammer tests, with the blade typically positioned in free–free or clamped–free boundary conditions, as well as the so-called pull and release tests [17–19], where the blade is in clamped–free conditions and it is pulled close to the free-end before being released to be able to measure its free-vibrations. The latter class involves output-only measurements with the purpose of collecting as much information as possible regarding the operational response of the structure. Implementation of a thorough monitoring at a dense set of structural locations, even those that are considered as hot spots, is often hindered by the inaccessibility of certain locations and the costs of sensors required, which might often limit the assessment procedure. Virtual Sensing (VS) can be exploited for estimating the response of the monitored blade at locations that are not instrumented for accessibility, time and costs limitations [20–22]. This technique combines a limited set of measurements with an updated Finite Element (FE) model of the structure in order to obtain an estimate of the quantities of interest, e.g strains, accelerations, displacements. The resulting "enriched" data can be used to build a true-to-life Digital Twin, able to reproduce representative dynamic response in operational circumstances.

In specific cases in which the main focus is on structural response reconstruction, Modal Expansion (ME) can be applied for VS to predict real-time operating data at unmeasured locations by mapping the measured responses through numerical normal modes. The prediction relies upon a modal decomposition of the measured responses to obtain the modal coordinates, which are expanded to the unmeasured Degrees of Freedom (DOFs) through the FE model mode shapes. This type of approach has been shown to provide robust predictions when applied on displacement or strain data acquired on simple structures, e.g. Base-Upright [23] and square plate [24] structures, while further demonstrated for a WT application on a purely accelerations-based dataset [25]. The latter has been also adopted in [26] for building virtual strain sensors for fatigue analysis of an offshore oil platform scaled mockup. Additionally, ME has been tested on both pure acceleration data and a mixed accelerations–strains dataset with the purpose of strain–stress estimation for fatigue-life prediction of an offshore monopile WT [27]. As an alternative to ME, Bayesian filtering has also been extensively adopted in the recent years for the purpose of VS [28–34]. In particular, Kalman-type filters were initially adopted for real-time state estimation under the assumption of complete knowledge of the loads acting on linear or even nonlinear structures [35–37]. Several extensions of the original algorithm have been proposed for linear dynamic systems in order to simultaneously tackle response prediction and inverse load identification. The so-called Augmented Kalman Filter (AKF) consists in including the unknown input within a new augmented state vector by assuming a pure random-walk model for its dynamics. The algorithm and its applicability to structural dynamics have been proposed in [38]. The AKF instability issues have been investigated in [39], where dummy measurements are adopted to overcome the un-observability of the augmented system matrix, which appears when acceleration measurements are exclusively considered. Numerical issues due to un-observability exhibited by the AKF have been resolved by an alternative algorithm for joint input-state estimation, commonly referred as the Dual Kalman Filter (DKF). The DKF, consisting in approaching the input and states prediction into two sequential stages under the assumption that the input follows a pure random-walk model, has been presented in [40] and tested in [41]. A more generic model for the input, i.e., a first order stationary autoregressive process, has been used in [28] to address joint input-state-parameter estimation via a combination of the DKF and the Unscented Kalman Filter (UKF) [42–45]. The need of an a priori assumption regarding the input dynamics has been overcome in [46] by the so-called Gillijn De Moore filter (GDF). This estimator is similar to the Kalman filter, except for the input true values being substituted by their optimal estimates. The GDF has been extended for systems with a direct transmission term in [47], while an improvement of the method regarding instabilities due to the number of adopted sensors exceeding the model order has been suggested in [48]. The input-state prediction through Bayesian VS often implies significant challenges when applied to complex systems subjected to uncertain loading conditions such as WTs. In order to address the reduction of these uncertainties, a substructure approach for input-state estimation has been proposed in [49] and validated on real data from an offshore WT in [50]. Recently, Bayesian filtering and ME have been combined via the so-called ME-AKF method. The latter consists in implementing strain responses predicted via ME into the AKF in order to enhance the online estimation results. The method has been proposed and tested on a full-scale rollercoaster structure in [51].

Within the context of Bayesian filtering, the assumption of a priori knowledge of the process and measurement noise statistics is placed. The process and measurement noise terms are used in a stochastic framework to reflect the uncertainties that stem from modeling errors/approximations, input uncertainty and measurement noise in the system representation. These two noise variables are commonly assumed to be independent, zero-mean white noise processes and the corresponding covariance matrices are treated as time-invariant quantities. The adoption of incorrect values for the process noise and measurement noise covariance matrices can lead to large estimation errors. In many cases, these values are not known exactly and offline tuning procedures are put in place [28,40,41,52–54]. In an effort to handle this, a common approach is to prescribe the measurement noise covariance by exploiting the available physical sensors specifications. Then, an optimization procedure regarding the process noise term is carried out in a rather heuristic manner, i.e., either by trial and error or by means of regularization metrics, such as the L-curve [55]. Besides its offline nature, this method often generates a plot which does not appear as a perfect L-shape. This renders the regularization parameter choice not straightforward for several Kalman-type filters, e.g. the AKF [38] and the DKF [41]. The application of regularization schemes is also limited to the condition in which only one parameter is to be calibrated. The working principle behind the L-curve has been adapted and used for simultaneously tuning more than one term in [30,56]. An online alternative to the previously mentioned methods for identifying the disturbances consists in using adaptive filtering techniques. These strategies have been applied for both the process and measurement noise terms [32] and they can be classified into four main categories [57]:

Bayesian [58], maximum-likelihood estimation [59], correlation [60–63] and covariance matching [64] methods. These approaches describe generic adaptive filtering schemes, which are typically characterized by excessive computational times. Moreover, the majority of these techniques are based on seeking the most suitable process and measurement noise covariance matrices steady-state estimates, rather then their current optimal values.

A more intuitive approach is proposed in this paper for adaptive process noise covariance matrix tuning for joint input-state estimation using the AKF. In this context, both the terms shaping the states and the unknown input uncertainties are taken into account for optimization. Moreover, the covariance matrix of the "augmented" process noise is considered to be time-variant, since the modeling uncertainty and the dynamic characteristics of the input (load) may vary in time. The newly proposed method, addressed as Adaptive-noise Augmented Kalman Filter (A-AKF), is based on reference response estimates computed using a combination of ME and Component Mode Synthesis [65] (CMS-ME). The A-AKF is tested on the input-state estimation of a 14.3 m long research blade manufactured by Olsen Wings. The mentioned research blade has been designed, tested and extensively studied [11] by DTU Wind Energy department in the framework of the project "BLATIGUE : Fast and efficient fatigue test of large wind turbine blades". In particular, focus is shed onto the input and strain response estimation during the so-called pull and release tests of the mentioned blade in clamped–free Boundary Conditions (BC).

The paper is organized as follows. Section 2 offers the formulation for the adopted Model Order Reduction (MOR) technique and the state-space equations for linear dynamical systems. Moreover, the AKF algorithm and a description of the A-AKF are reported in Section 2. Section 3 introduces the case study analyzed within this work. Next, Section 4 validates the CMS-ME approach used as reference within the proposed adaptive framework by offering the response predictions for the analyzed case study and comparing them with the standard ME results. Section 4 continues reporting the analysis of the input–response predictions achieved by the conventional AKF for several choices of the time-invariant process noise covariance associated to the unknown input. The input–response predictions produced by the A-AKF are then proposed in Section 4, along with a parametric assessment of the method and a comparison with the results achieved via the conventional AKF and the CMS-ME approach. Finally, the work is concluded in Section 5.

2. Theoretical background

2.1. Problem formulation

The equation of motion of a linear structural system, which is simulated via use of a FE model, may be formulated as a second order vector differential equation of the form:

$$\mathbf{M}\ddot{\mathbf{z}}(t) + \mathbf{D}\dot{\mathbf{z}}(t) + \mathbf{K}\mathbf{z}(t) = \mathbf{S}_i\mathbf{u}(t) \tag{1}$$

where $\mathbf{z}(t) \in \mathbb{R}^{n_{dof}}$ is the vector of displacements, corresponding to the FE model DOFs, $\mathbf{M} \in \mathbb{R}^{n_{dof}\times n_{dof}}$, $\mathbf{D} \in \mathbb{R}^{n_{dof}\times n_{dof}}$ and $\mathbf{K} \in \mathbb{R}^{n_{dof}\times n_{dof}}$ denote the mass, damping and stiffness matrices respectively; $\mathbf{u}(t) \in \mathbb{R}^{n_i}$ (with n_i representing the number of loads) is the input vector and $\mathbf{S}_i \in \mathbb{R}^{n_{dof}\times n_i}$ is the Boolean input shape matrix that selects the DOFs where loads (inputs) are applied.

A MOR technique, relying on Component Mode Synthesis (CMS), as described in [65], can be applied to reduce the model size. According to this method, the dynamic behavior of a structure can be formulated as a superposition of modal contributions:

$$\mathbf{z} \approx \mathbf{\Psi}\mathbf{p} \tag{2}$$

where $\mathbf{\Psi} \in \mathbb{R}^{n_{dof}\times n_r}$ is the reduction basis and $\mathbf{p} \in \mathbb{R}^{n_r}$ is the vector of the generalized coordinates of the system, with n_r being the dimension of the reduced coordinates.

Inserting the reduction basis into Eq. (1), it results in:

$$\mathbf{M}_r\ddot{\mathbf{p}}(t) + \mathbf{D}_r\dot{\mathbf{p}}(t) + \mathbf{K}_r\mathbf{p}(t) = \mathbf{S}_r\mathbf{u}(t) \tag{3}$$

where the mass, damping, stiffness and input shape matrices of the reduced system are respectively $\mathbf{M}_r = \mathbf{\Psi}^{\mathbf{T}}\mathbf{M}\mathbf{\Psi}$, $\mathbf{D}_r = \mathbf{\Psi}^{\mathbf{T}}\mathbf{D}\mathbf{\Psi}$, $\mathbf{K}_r = \mathbf{\Psi}^{T}\mathbf{K}\mathbf{\Psi}$ and $\mathbf{S}_r = \mathbf{\Psi}^{\mathbf{T}}\mathbf{S}_i$.

The adopted reduction basis can be expressed as:

$$\mathbf{\Psi} = \begin{bmatrix}\mathbf{\Psi}_n & \mathbf{\Psi}_\alpha\end{bmatrix}; \tag{4}$$

where $\mathbf{\Psi}_n \in \mathbb{R}^{n_{dof}\times n_k}$ is the matrix of the numerical normal modes to be included in the Reduced Order Model (ROM), i.e., the eigenmodes of the entire structure in the frequency range of interest, and $\mathbf{\Psi}_\alpha \in \mathbb{R}^{n_{dof}\times n_\alpha}$ is the residual attachment modes matrix. The residual attachment modes are usually inserted in this kind of reduction bases in order to include a representation of the static response of the structure to an input at a specific DOF. Typically, for each load acting on the structure, the relative residual attachment mode is included in the basis. The latter is computed as a mode of the structure under application of a unitary static input applied at the actual input DOF. Therefore, n_α is equal to the number of loads applied to the system and $n_r = n_k + n_\alpha$.

Within a filtering context, it is useful to employ the state-space representation of Eq. (1):

$$\begin{cases}\dot{\mathbf{x}}(t) = \mathbf{A}\mathbf{x}(t) + \mathbf{B}\mathbf{u}(t)\\ \mathbf{y}(t) = \mathbf{C}\mathbf{x}(t) + \mathbf{G}\mathbf{u}(t)\end{cases} \tag{5}$$

where $\mathbf{x} = \begin{bmatrix}\mathbf{p} & \dot{\mathbf{p}}\end{bmatrix}^T \in \mathbb{R}^{2n_r}$ is the state vector. Matrices $\mathbf{A}$ and $\mathbf{B}$ are computed as functions of $\mathbf{M}_r$, $\mathbf{K}_r$ and $\mathbf{D}_r$:

$$\mathbf{A} = \begin{bmatrix} \mathbf{0}_{n_r} & \mathbf{I}_{n_r} \\ -\mathbf{M}_r^{-1}\mathbf{K}_r & -\mathbf{M}_r^{-1}\mathbf{D}_r \end{bmatrix}, \qquad \mathbf{B} = \begin{bmatrix} \mathbf{0}_{n_r \times n_i} \\ \mathbf{M}_r^{-1}\mathbf{S}_r \end{bmatrix}. \tag{6}$$

The second equation of Eq. (5) defines the system measurements, with $\mathbf{y} \in \mathbb{R}^{n_o}$ representing the observations vector, while the time-invariant matrices $\mathbf{C} \in \mathbb{R}^{n_o \times 2n_r}$ and $\mathbf{G} \in \mathbb{R}^{n_o \times n_i}$ are constructed as follows:

$$\mathbf{C} = \begin{bmatrix} \mathbf{S}_d & \mathbf{0}_{n_d \times n_r} \\ \mathbf{0}_{n_v \times n_r} & \mathbf{S}_v \\ -\mathbf{S}_a\mathbf{M}_r^{-1}\mathbf{K} & -\mathbf{S}_a\mathbf{M}_r^{-1}\mathbf{D}_r \end{bmatrix}, \qquad \mathbf{G} = \begin{bmatrix} \mathbf{0}_{n_d \times n_i} \\ \mathbf{0}_{n_v \times n_i} \\ \mathbf{S}_a\mathbf{M}_r^{-1}\mathbf{S}_r \end{bmatrix}, \tag{7}$$

The output vector $\mathbf{y}$ may contain n_d displacement or strain, n_v velocity and n_a acceleration measurements at specific DOFs, which are respectively selected via the matrices $\mathbf{S}_d \in \mathbb{R}^{n_d \times n_r}$, $\mathbf{S}_v \in \mathbb{R}^{n_v \times n_r}$, and $\mathbf{S}_a \in \mathbb{R}^{n_a \times n_r}$. For strain measurements, the $\mathbf{S}_d$ matrix is constructed through a combination of DOFs. Using the finite element formulation, the strain vector ε at any point of an element can be expressed as a function of the displacement vector $\mathbf{z}$ via the following formula:

$$\boldsymbol{\varepsilon} = S\mathbf{z} \tag{8}$$

where S is a differential operator defined as follows:

$$S = \begin{bmatrix} \frac{\partial}{\partial x} & 0 & 0 \\ 0 & \frac{\partial}{\partial y} & 0 \\ 0 & 0 & \frac{\partial}{\partial z} \\ \frac{\partial}{\partial y} & \frac{\partial}{\partial x} & 0 \\ 0 & \frac{\partial}{\partial z} & \frac{\partial}{\partial y} \\ \frac{\partial}{\partial z} & 0 & \frac{\partial}{\partial x} \end{bmatrix}. \tag{9}$$

The displacement vector $\mathbf{z}$ at each element point can be discretized as follows:

$$\mathbf{z} \approx \sum_a N^a \mathbf{z}^a \tag{10}$$

where $\mathbf{z}^a$ is the displacement vector at the ath node of the element and N^a are the element shape functions. By introducing Eq. (10) and (2) into Eq. (8), the following expression for the strain vector is obtained:

$$\boldsymbol{\varepsilon} = \sum_a \mathbf{B}^a \boldsymbol{\Psi}^a \mathbf{p} \tag{11}$$

where $\boldsymbol{\Psi}^a$ is the reduction basis computed at the element nodal DOFs and $\mathbf{B}^a$ contains the shape functions derivatives:

$$\mathbf{B}^a = \begin{bmatrix} \frac{\partial N^a}{\partial x} & 0 & 0 \\ 0 & \frac{\partial N^a}{\partial y} & 0 \\ 0 & 0 & \frac{\partial N^a}{\partial z} \\ \frac{\partial N^a}{\partial y} & \frac{\partial N^a}{\partial x} & 0 \\ 0 & \frac{\partial N^a}{\partial z} & \frac{\partial N^a}{\partial y} \\ \frac{\partial N^a}{\partial z} & 0 & \frac{\partial N^a}{\partial x} \end{bmatrix}. \tag{12}$$

Therefore, when the output vector $\mathbf{y}$ contains strain measurements, the selection matrix $\mathbf{S}_d$ is obtained evaluating the matrix $\sum_a \mathbf{B}^a \boldsymbol{\Psi}^a$ at the strain vector components corresponding to the measured strain quantity.

When the structure is only excited by unknown loads $\mathbf{u}$, the augmented state vector $\mathbf{x}^a \in \mathbb{R}^{2n_r + n_i}$ can be built as follows:

$$\mathbf{x}^a = \begin{bmatrix}\mathbf{x} & \mathbf{u}\end{bmatrix}^T. \tag{13}$$

In order to shape the unknown loads contained in the input vector $\mathbf{u}$ as states, the augmented representation in Eq. (14) is required for the state-space system in Eq. (5).

$$\begin{cases} \dot{\mathbf{x}}^a(t) = \mathbf{A}^a \mathbf{x}^a(t) \\ \mathbf{y}(t) = \mathbf{C}^a \mathbf{x}^a(t) \end{cases}, \qquad \mathbf{A}^a = \begin{bmatrix} \mathbf{A} & \mathbf{B} \\ \mathbf{0} & \mathbf{I} \end{bmatrix}, \qquad \mathbf{C}^a = \begin{bmatrix}\mathbf{C} & \mathbf{G}\end{bmatrix}, \tag{14}$$

where $\mathbf{A}^a \in \mathbb{R}^{n_{aug} \times n_{aug}}$ is the augmented system matrix and $\mathbf{C}^a \in \mathbb{R}^{n_o \times n_{aug}}$ is the augmented output matrix, with $n_{aug} = 2n_r + n_i$. In Eq. (14), a zeroth-order random-walk model [38,66,67] has been adopted to model the input dynamics due to lack of prior information regarding the loads acting on the structure. The time-discrete version of the input (load) random-walk model is:

$$\mathbf{u}_k = \mathbf{u}_{k-1} + \mathbf{w}_{k-1}^u \tag{15}$$

where $\mathbf{w}^u$ is a vector of zero-mean white uncorrelated processes with associated covariance matrix $\mathbf{Q}^u \in \mathbb{R}^{n_i \times n_i}$. Hence, the diagonal elements of $\mathbf{Q}^u$ represent the variance of the unknown inputs increments in time.

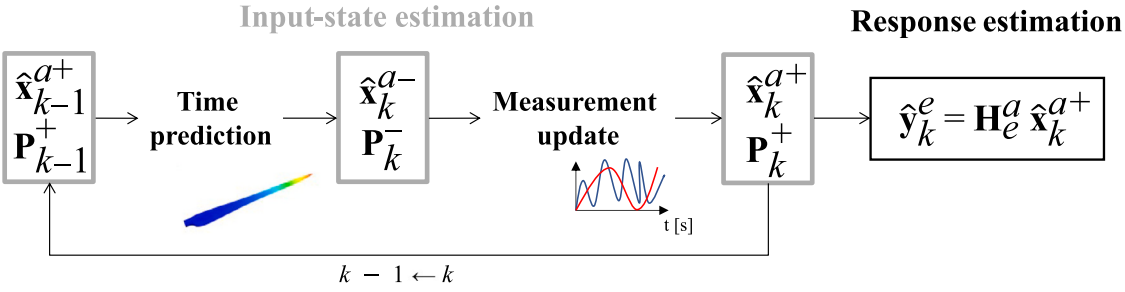

Fig. 1. AKF algorithm scheme.

Translating Eq. (14) from the continuous to the time-discrete state-space form, the following formulation can be derived:

$$\begin{cases} \mathbf{x}_k^a = \mathbf{F}^a \mathbf{x}_{k-1}^a + \mathbf{w}_{k-1}^a \\ \mathbf{y}_k = \mathbf{H}^a \mathbf{x}_k^a + \mathbf{v}_k \end{cases} . \tag{16}$$

In Eq. (16), stationary mutually uncorrelated zero-mean white noises $\mathbf{w}$ and $\mathbf{v}$ have been introduced to respectively take into account model uncertainties and measurement noise. The whiteness assumption for $\mathbf{w}^u$, $\mathbf{w}$ and $\mathbf{v}$ excludes the presence of systematic uncertainties affecting the unknown input, the model and the measurements, respectively. The associated noise covariance matrices are $\mathbf{R} \in \mathbb{R}^{n_o \times n_o} = \mathbb{E}\{\mathbf{v}_k \mathbf{v}_l^T\} \geq 0$ for measurement noise and $\mathbf{Q}^a \in \mathbb{R}^{n_{aug} \times n_{aug}} = \mathbb{E}\{\mathbf{w}_k^a \mathbf{w}_l^{aT}\} = \begin{bmatrix} \mathbf{Q} & \mathbf{0} \\ \mathbf{0} & \mathbf{Q}^u \end{bmatrix} \geq 0$ for process noise, where matrix $\mathbf{Q} \in \mathbb{R}^{2n_r \times 2n_r} = \mathbb{E}\{\mathbf{w}_k \mathbf{w}_l^T\}$ takes into account uncertainties related to the system states.

Eqs. (13) and (16) indicate that the input location has to be known in order to build the augmented state-space representation. In Eq. (16), the output matrix is obtained as $\mathbf{H}^a = \begin{bmatrix} \mathbf{C} & \mathbf{G} \end{bmatrix}$, while matrix $\mathbf{F}^a$ formulation depends on the chosen discretization scheme. An exponential time integration scheme [68] has been adopted for this application.

2.2. The augmented Kalman filter for joint input-state estimation

The discrete-time formulation of the AKF can be split into two sequential steps as follows:

1. Time Prediction:

$$\hat{\mathbf{x}}_k^{a-} = \mathbf{F}^a \hat{\mathbf{x}}_{k-1}^{a+} \tag{17}$$

$$\mathbf{P}_k^- = \mathbf{F}^a \mathbf{P}_{k-1}^+ \mathbf{F}^{aT} + \mathbf{Q}^a \tag{18}$$

2. Measurement Update:

$$\mathbf{K}_k = \mathbf{P}_k^- \mathbf{H}^{aT} \left(\mathbf{H}^a \mathbf{P}_k^- \mathbf{H}^{aT} + \mathbf{R} \right)^{-1} \tag{19}$$

$$\hat{\mathbf{x}}_k^{a+} = \hat{\mathbf{x}}_k^{a-} + \mathbf{K}_k \left(\mathbf{y}_k - \mathbf{H}^a \hat{\mathbf{x}}_k^{a-} \right) \tag{20}$$

$$\mathbf{P}_k^+ = \left(\mathbf{I} - \mathbf{K}_k \mathbf{H}^a \right) \mathbf{P}_k^- \tag{21}$$

where $\mathbf{P}_k = \mathbb{E}\{ \left(\mathbf{x}_k^a - \hat{\mathbf{x}}_k^a \right) \left(\mathbf{x}_k^a - \hat{\mathbf{x}}_k^a \right)^T \}$ is the estimate covariance matrix, also known as error covariance matrix; a measure of the estimated accuracy of the state estimate. The minimization of the $\mathbf{P}_k$ matrix trace forms the working principle of the AKF, which is presented in Fig. 1 through a block diagram scheme.

In particular, the time prediction step propagates the augmented state vector $\hat{\mathbf{x}}_k^{a-}$ and the error covariance matrix $\mathbf{P}_k^-$ from $k-1$ to k through the augmented state-space system, which can be retrieved from the structure FE model. The resulting prediction is then corrected by the measurement update step, which uses information given by the available observations at time step k to build the augmented state vector posterior estimate $\hat{\mathbf{x}}_k^{a+}$ and the corresponding posterior estimate covariance matrix $\mathbf{P}_k^+$. Once the estimated augmented state vector $\hat{\mathbf{x}}_k^{a+}$ has been obtained, it can be used for predicting the vector $\hat{\mathbf{y}}_k^e$ of the n_e unmeasured responses using the following formula:

$$\hat{\mathbf{y}}_k^e = \mathbf{H}_e^a \hat{\mathbf{x}}_k^{a+} \tag{22}$$

where $\mathbf{H}_e^a$ is the augmented output matrix computed at the DOFs where the response has to be estimated.

The AKF forms a class of Bayesian estimators that has been extensively adopted for the task of joint input-state estimation, meaning the simultaneous estimation of both unmeasured response (state) and unknown loads (inputs) acting on structures. It has been demonstrated that the performance of Bayesian estimators is highly dependent on the available prior information regarding model uncertainties and measurement noise levels. The noise covariance matrices associated with these two terms, i.e., $\mathbf{Q}^a$ for the process noise and $\mathbf{R}$ for the measurement noise, are often treated as tuning parameters of the filter, which can be adjusted

heuristically in order to obtain satisfactory estimates. While information on $\mathbf{R}$ matrix can on some level be retrieved on the basis of the sensor precision, as defined by its specifications, the availability of prior information on the process matrix, $\mathbf{Q}^a$, represents an obvious challenge.

Within the present work, focus will be placed on building an automated procedure for adaptively tuning the time-variant process noise covariance with the purpose of optimizing predictions of the quantities of interest.

2.3. Process noise covariance tuning

When joint input-state estimation is pursued, the augmented process noise covariance matrix can be written as a block diagonal matrix $\mathbf{Q}^a = \begin{bmatrix} \mathbf{Q} & \mathbf{0} \\ \mathbf{0} & \mathbf{Q}^u \end{bmatrix} \geq 0$, such that $\mathbf{Q}\delta_{kl}$ with $1 \leq k,l \leq 2n_r$ and $\mathbf{Q}^u\delta_{kl}$ with $1 \leq k,l \leq n_i$ under the assumption of uncorrelated noise sources. While the diagonal elements of $\mathbf{Q}$ are typically assigned a constant value that is very low when compared against the order of magnitude of the state vector, the process noise covariance matrix $\mathbf{Q}^u$ associated to the unknown input is treated as a regularization matrix when joint input-state estimation is performed through the AKF. This common practice derives from the dependence of the smoothness of the estimation on $\mathbf{Q}^u$, which can be therefore tuned to tackle the ill-conditioning of the problem [38,39,69]. In doing so, the resulting diagonal elements of $\mathbf{Q}^u$, i.e., the uncertainty related to the unknown inputs, is typically higher than the one associated to the regular states (reflecting mostly modeling errors).

We here demonstrate, by means of the analyzed experimental case study, that a simultaneous tuning of $\mathbf{Q}$ and $\mathbf{Q}^u$ can instead improve the prediction results. The diagonal elements of $\mathbf{Q}^u$ are commonly assigned by either setting a standard regularization parameter estimation, e.g. the L-curve [55], or via trial and error. The latter depends on the user expertise and does not provide a unique solution to the problem. On the other hand, the L-curve does not exhibit its standard L-shape when used for input-state estimation via use of the AKF with experimental data [38,41,70], which renders the estimation of the regularization parameter user-dependent. This behavior is commonly not encountered for fully simulated data sets in absence of process noise [71,72]. It is also worth noting that regularization parameter values obtained through the L-curve are related to the optimal estimates of the measured responses, which do not necessarily imply optimized predictions for the unmeasured quantities. Moreover, both the L-curve and the trial and error schemes may only be applied in an offline fashion, preventing real-time applicability. An online alternative consists in using techniques based on adaptive filtering schemes [57] developed for generic use of Kalman-type filters. These approaches imply high computational effort and require adaptation to the specific estimator and application domain. Moreover, they are often limited to the identification of steady-state estimates of both the process and the measurement noise covariance matrices.

2.3.1. Adaptive-noise augmented Kalman filter

In this work, an automated procedure for estimating the optimal $\mathbf{Q}^a$ matrix for joint input-state estimation in a near-online fashion is proposed. The matrix optimality expression is based on the minimization of an overall error estimate which takes into account the prediction inaccuracy of the quantities of interest, i.e., unknown input vector and measured and unmeasured responses. The process relies on the following assumptions:

- The process noise covariance $\mathbf{Q}$ is assumed to be fully determined by two parameters, i.e., two distinct covariance values respectively assigned across all the displacement and all the velocity components of the state vector. This assumption allows to adopt different noise levels for displacement and velocity components in order to account for their amplitude discrepancy. On the other hand, a different input process noise covariance component is assigned to each unknown load entry. Matrices $\mathbf{Q}$ and $\mathbf{Q}^u$ can be expressed as $\mathbf{Q} = \begin{bmatrix} q^{n_d}\mathbf{I} & \mathbf{0} \\ \mathbf{0} & q^{n_v}\mathbf{I} \end{bmatrix}$ with $\mathbf{I} \in \mathbb{R}^{n_r \times n_r}$ and $\mathbf{Q}^u = \mathbf{q}^u\mathbf{I}$ with $\mathbf{I} \in \mathbb{R}^{n_i \times n_i}$ and $\mathbf{q}^u = \begin{bmatrix} q_1^u \dots q_{n_i}^u \end{bmatrix}^T$. For the sake of simplicity, the situation in which the structure is subjected to a single excitation source is considered in what follows. While the reported methodology will thus address three scalar quantities q^{n_d}, q^{n_v} and q^u, it should be stated that it is straightforward to generalize for more excitation sources. The procedure can be easily extended for the case of multiple loads by including all the elements of $\mathbf{q}^u$ in the set of scalar quantities to be optimally selected.
- The standard $\mathbf{Q}^a$ matrix estimation procedure treats this matrix as time-invariant, implying that the same expression is adopted for the AKF at each kth iteration [33,41,55,56]. To the contrary, the hereby proposed methodology assumes a time-variant $\mathbf{Q}^a$ matrix, which is updated every N time-steps. This hypothesis allows to select the optimal augmented process noise covariance matrix in near real-time, allowing to perform input-state prediction while measurements acquisition is running.
- The proposed approach does not require user intervention, except for an a priori assumption regarding the ranges within which q^{n_d}, q^{n_v} and q^u can vary: $q_{min}^{n_d} \leq q^{n_d} \leq q_{max}^{n_d}$, $q_{min}^{n_v} \leq q^{n_v} \leq q_{max}^{n_v}$ and $q_{min}^u \leq q^u \leq q_{max}^u$.

The herein presented methodology can be applied starting from the a priori selected bounds for q^{n_d}, q^{n_v} and q^u. Suitable values for each variable are sampled in the assigned range on a logarithmic uniformly distributed scale. In order to ensure that the displacement and velocity components are differentiated, the ranges associated to q^{n_d} and q^{n_v} are set to be equivalent and a constraint between the corresponding sampled values within these ranges is imposed. M combinations of q^{n_d}, q^{n_v} and q^u, i.e., M distinct $\mathbf{Q}^a$ matrices, can be derived from the sampled values. Fig. 2 shows a block diagram scheme for the developed A-AKF.

The algorithm operates by running a bank of filters (AKF) in parallel, one for each of the generated M $\mathbf{Q}^a$ samples, for N time-steps. For the N-steps window, the overall error estimate $\bar{E}$ reported in Eq. (32) is computed for each candidate AKF and minimized to select the optimal $\mathbf{Q}^a$. The latter is adopted to derive the best estimates for the state vector, error covariance matrix and responses throughout the N-steps window. The estimated $\hat{\mathbf{x}}_{k+N}^{a+}$ and $\mathbf{P}_{k+N}^{+}$ are used as input for the estimation at step $k+N+1$.

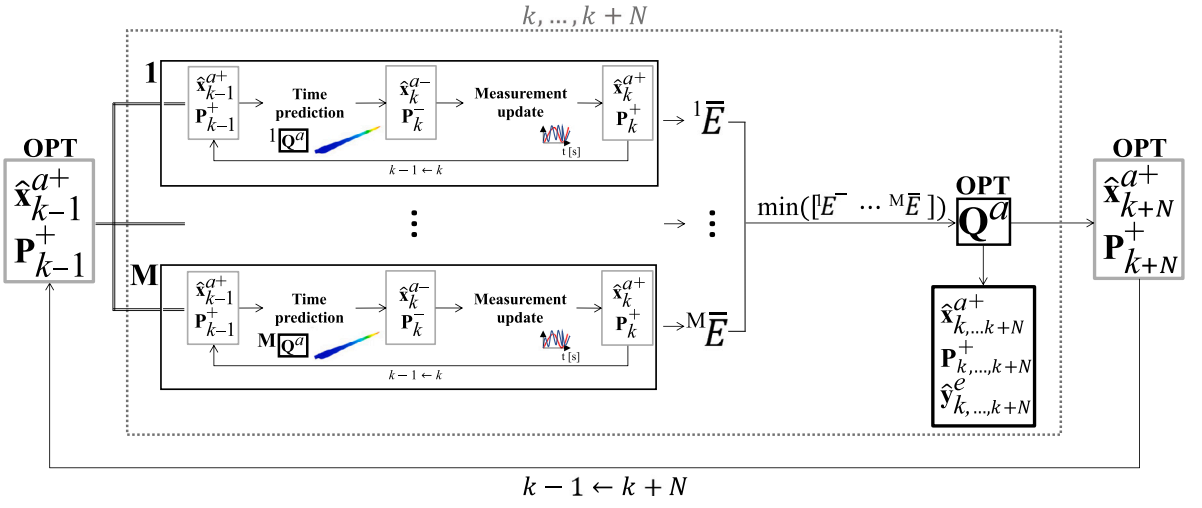

Fig. 2. Adaptive-noise Augmented Kalman Filter scheme.

The employed error quantification for each of the parallely run filters needs to account for imprecision in both the input and measured/unmeasured response estimates during the N-steps batch. To what concerns the response estimates, prediction can be performed via Eq. (22) for both the measured (observed) quantities $\hat{\mathbf{y}}^o_{k,\dots,k+N}$ and the fully predicted ones $\hat{\mathbf{y}}^e_{k,\dots,k+N}$ by selecting the appropriate output matrix. As shown in the structure that is described next, estimated quantities for both the measured and unmeasured responses are taken into account in the error quantification equation, offering global insights into the AKF response prediction accuracy during the analyzed time window. The adopted error estimate for the unknown input, the re-estimated observations and the predicted responses for each N-steps window are reported next.

Prediction error for the Measured Quantities

The prediction inaccuracy regarding the measured (observed) quantities can be straightforwardly quantified by means of the following estimate:

$$E^o = \frac{1}{n_o}\sqrt{\sum_{l=1}^{n_o}\left(\text{argmin}_\theta \|\theta \mathbf{y}^o_l - (\mathbf{y}^o_l - \hat{\mathbf{y}}^o_l)\|_2\right)^2} \tag{23}$$

where $\mathbf{y}^o_l = \left[y^o_{l_1} \cdots y^o_{l_j} \cdots y^o_{l_N}\right]$ is the response acquired at the lth measured DOF, i.e., $1 \le l \le n_o$, during the current window ($1 \le j \le N$). Similarly, $\hat{\mathbf{y}}^o_l = \left[\hat{y}^o_{l_1} \cdots \hat{y}^o_{l_j} \cdots \hat{y}^o_{l_N}\right]$ is the response re-estimated by the AKF at the lth measured DOF at the N time-steps within the current time batch. The term θ in Eq. (23) is the scalar result of the least-squares solution of a system of linear equations $\theta \mathbf{y}^o_l = (\mathbf{y}^o_l - \hat{\mathbf{y}}^o_l)$ for the lth measured response, where $\mathbf{y}^o_l \in \mathbb{R}^N$ and $(\mathbf{y}^o_l - \hat{\mathbf{y}}^o_l) \in \mathbb{R}^N$. The latter vector quantifies the deviation between the re-estimated and the measured signals at each time-step, while the vector $\mathbf{y}^o_l$ is used to normalize this deviation in order to get a dimensionless estimate. The least-squares formulation in Eq. (23) has been preferred to other types of estimates, e.g., mean value of N instantaneous errors, since it allows for a smoothed error estimate over the N time-steps which guarantees stable input and response predictions for large q^{n_d}, q^{n_v} and q^u range bounds. This exempts the A-AKF user from the need of selecting ad-hoc bounds for the variables to be tuned.

Prediction error for the Unmeasured Quantities

In order to quantify the prediction error for the unmeasured (predicted) response quantities, the formulation in Eq. (23) can be reformulated as follows:

$$E^p = \frac{1}{n_e}\sqrt{\sum_{l=1}^{n_e}\left(\text{argmin}_\beta \|\beta \mathbf{y}^e_l - (\mathbf{y}^e_l - \hat{\mathbf{y}}^e_l)\|_2\right)^2} \tag{24}$$

where $\hat{\mathbf{y}}^e_l = \left[\hat{y}^e_{l_1} \cdots \hat{y}^e_{l_j} \cdots \hat{y}^e_{l_N}\right]$ is the response estimated by the AKF during the current window at the lth unmeasured DOF, i.e., $1 \le l \le n_e$, and $\mathbf{y}^e_l$ is its actual value. Being the latter quantity not available, a reference estimate can be used as an alternative.

The present work proposes the coupling of the CMS and ME schemes for building an instantaneous reference vector to quantify inaccuracy in the virtually sensed (unmeasured) responses. Following application of the ME technique, the numerical normal modes matrix $\boldsymbol{\Psi}_n$ can be expressed by distinguishing the measured (observed) and unmeasured (predicted) DOFs as follows:

$$\boldsymbol{\Psi}_n = \begin{bmatrix}\boldsymbol{\Psi}^o_n \\ \boldsymbol{\Psi}^p_n\end{bmatrix}; \tag{25}$$

with $\boldsymbol{\Psi}_n^o \in \mathbb{R}^{n_o \times n_k}$ and $\boldsymbol{\Psi}_n^p \in \mathbb{R}^{n_p \times n_k}$, where $n_p = n_{dof} - n_o$. The $\boldsymbol{\Psi}_n^o$ matrix is obtained via the following formulas for displacement or strain, velocity and acceleration measurements, respectively: $\boldsymbol{\Psi}_n^o = \mathbf{S}_d \boldsymbol{\Psi}_n$, $\boldsymbol{\Psi}_n^o = \mathbf{S}_v \boldsymbol{\Psi}_n$ and $\boldsymbol{\Psi}_n^o = \mathbf{S}_a \boldsymbol{\Psi}_n$. When specifically adopted for strain measurements, the selection matrix $\mathbf{S}_d$ is obtained evaluating the matrix $\sum_a \mathbf{B}^a \boldsymbol{\Psi}^a$ (derived in Section 2.1) at the strain vector components corresponding to the measured strain quantity.

When a high correlation between the numerical and the experimental mode shapes is available, measured responses can be used to determine the modal displacement (or its first and second derivative in case of velocity and acceleration measurements, respectively) at any DOF of the structure. This approach is valid for any type of response, e.g., displacement, strain, velocity, acceleration [27]. Specifically, it can be adopted for real-time estimation if the measured and estimated quantities are of the same type, as demonstrated in [25]. If one would use a certain type of measurement, e.g. acceleration, to estimate a different type of response, e.g., displacement, the formulation would require integration or the use of a frequency domain approach via the Fourier transform of Eq. (7), which would render the method not suitable for real-time prediction. Within this work, only one type of response, i.e., strain, will be considered. However, it is worth to notice that the method can in any case be used as reference within the A-AKF as the response prediction errors are computed over N time-steps windows. For the sake of simplicity and for consistency with the analyzed case study, the hereby reported formulation will refer to displacement-level measurements.

In this work, the generalized coordinates introduced in Eq. (2) via use of the CMS reduction basis $\boldsymbol{\Psi}$ will be adopted instead of the conventional modal coordinates. By defining the measured DOFs as $\mathbf{z}^o(t)$ and the estimated DOFs as $\mathbf{z}^p(t)$, the relationship in Eq. (2) can be written for only the n_o measured DOFs as:

$$\mathbf{z}_k^o = \boldsymbol{\Psi}^o \mathbf{p}_k \tag{26}$$

where vectors $\mathbf{z}^o(t)$ and $\mathbf{p}(t)$ have been transferred from continuous to discrete-time representation for the sake of consistency with the proposed notation. From Eq. (26), the generalized coordinates vector $\mathbf{p}_k$ can be expressed as:

$$\mathbf{p}_k = (\boldsymbol{\Psi}^{oT} \boldsymbol{\Psi}^o)^{-1} \boldsymbol{\Psi}^{oT} \mathbf{z}_k^o = \boldsymbol{\Psi}^{o\dagger} \mathbf{z}_k^o. \tag{27}$$

It is worth mentioning that Eq. (27) can be solved as a determined (or overdetermined) system only when the number of measurements n_o is equal to (or greater than) the number of modes included in the reduction basis, i.e., n_k for ME and n_r for CMS-ME.

The prediction at unmeasured DOFs can be obtained by expanding the generalized coordinates vector computed in Eq. (27):

$$\hat{\mathbf{z}}_k^p = \boldsymbol{\Psi}^p \mathbf{p}_k = \boldsymbol{\Psi}^p \boldsymbol{\Psi}^{o\dagger} \mathbf{z}_k^o. \tag{28}$$

The proposed CMS-ME approach can be adopted for predicting any dynamic response quantity, i.e., displacement, acceleration, or strain, by using an appropriate reduction basis. The vector $\hat{\mathbf{z}}_k^p$ of the responses estimated via CMS-ME can then be used as a reference for computing the AKF prediction error as:

$$E^p = \frac{1}{n_e} \sqrt{\sum_{l=1}^{n_e} \left(\operatorname{argmin}_\beta \| \beta \hat{\mathbf{z}}_l^p - (\hat{\mathbf{z}}_l^p - \hat{\mathbf{y}}_l^e) \|_2 \right)^2} \tag{29}$$

where $\hat{\mathbf{z}}_l^p = \left[\hat{z}_{l_1}^p \cdots \hat{z}_{l_j}^p \cdots \hat{z}_{l_N}^p \right]$ and $\hat{\mathbf{y}}_l^e$ are the responses respectively estimated by the CMS-ME approach and the AKF at the lth unmeasured DOF, i.e., $1 \le l \le n_e$, during the current time batch ($1 \le j \le N$).

Prediction error for Unknown Input

When the AKF is adopted for input-state estimation, the input estimation error is intrinsically contained in the error covariance matrix $\mathbf{P}$. The latter is indeed defined as:

$$\mathbf{P} = \begin{bmatrix} \mathbf{P}^{nn} & \mathbf{P}^{nu} \\ \mathbf{P}^{un} & \mathbf{P}^{uu} \end{bmatrix} \tag{30}$$

where $\mathbf{P}^{uu} = \mathbb{E}\{(\mathbf{u} - \hat{\mathbf{u}})(\mathbf{u} - \hat{\mathbf{u}})^T\} \in \mathbb{R}^{n_i \times n_i}$ expresses the covariance of the unknown input error. For the sake of clarity, the explicit time dependency in Eq. (30) has been omitted. The diagonal elements of this matrix represent the variance of each unknown input estimation error. The error term for a single input prediction $\hat{u}$, during the current N-steps window, is therefore expressed as follows:

$$E^u = \sqrt{\frac{1}{N} \sum_{j=k}^{k+N} \frac{P_j^{uu}}{\hat{u}_j^2}} \tag{31}$$

where the squared amplitude of the corresponding estimated input at each jth time-step within the window $\hat{u}_j^2$ has been used for normalization. By considering zero cross-correlation of noise sources, or in other words zero diagonal entries for $\mathbf{P}^{uu}$, the hereby presented approach works under the assumption that negligible cross-correlation terms (both between the various inputs and between the states and the inputs) are encountered. It is worth noting that adjustments of the method may be needed in case large off-diagonal terms are expected in the $\mathbf{P}$ matrix. In Eqs. (23), (29) and (31), the square root has been introduced in order to respect the dimensionality of the absolute quantity to which the error is referring, i.e., uE for the strain responses and N for the input.

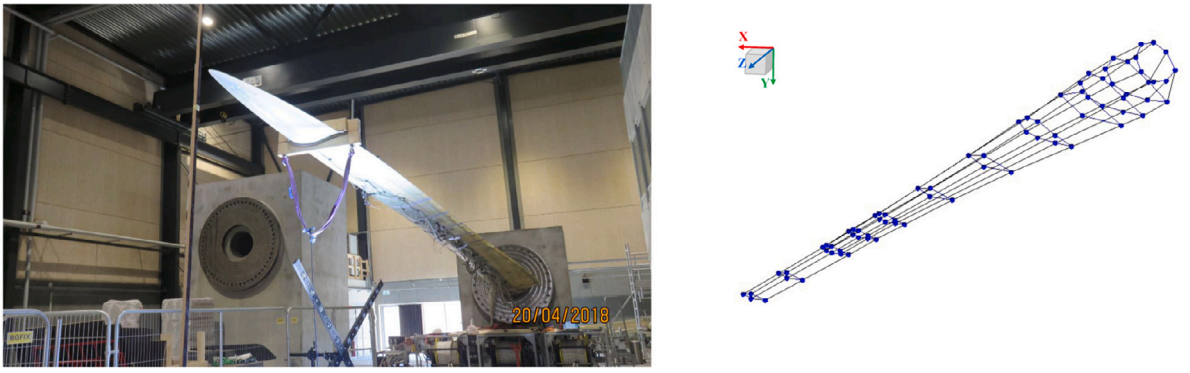

Fig. 3. WT blade setup during the pull and release test (left). Test geometry (right).

Overall Error Estimate

Considering the vector $\mathbf{E} = \begin{bmatrix} E^o & E^p & E^u \end{bmatrix}^T$, the overall inaccuracy estimate for the current time window is defined as:

$$\bar{E} = \|\mathbf{E}\|_2. \tag{32}$$

In case of multiple excitation sources, the error E^u computed for each input can be included in the vector $\mathbf{E}$.

3. Case study: WT blade output-only measurements

Output-only measurements on WT blades can be exploited with the purpose of establishing a dynamic virtualization process, which could be considered to evolve in real-time, provided that the employed algorithms can be applied online or near-online. During this type of test campaigns, structural response is acquired at a finite (limited) number of locations. Bayesian filtering (i) allows to extend the information from a few sensed locations to the entire full-field blade response and (ii) delivers an estimate of the unmeasured loads acting on the blade. The AKF thus offers a tool with the potential to operate in real-time, employing fusion of the measured data with a numerical (FE-based) model of the system, thus delivering a hybrid model, suited for virtualization. This process can be installed throughout the life-cycle of WT blades (including operational conditions) for enabling a continuous performance evaluation with the purpose of lifetime prediction and predictive maintenance.

The presented experimental case study includes pull and release tests on a 14.3 m long research blade made of glass fiber reinforced plastics. The WT blade was entirely designed by DTU Wind Energy and manufactured by Olsen Wings in the framework of the "BLATIGUE" project. The DTU Wind Energy department has kindly provided the FE model of the blade required for the present work, along with the experimental data this work refers to.

3.1. Pull and release tests

As shown in Fig. 3 (left), during the hereby considered pull and release tests, the blade was clamped to a rigid steel-reinforced concrete block through the circular interface plate in a flapwise configuration. The test consisted in pulling the blade downward by making use of a bungee applied at a distance of 13.1 m from the clamping. Once the blade tip had reached the desired displacement, the blade was released and the free vibration response recorded. The load time history has not been acquired. Nevertheless, the scalar value of the static load applied right before the release instant is available. The blade was instrumented via 76 strain gauges distributed on 12 sections along its length, all measuring along the axial direction of the blade (z-axis in Fig. 3). Each instrumented section includes 4 or 8 strain gauges. The sensors configuration is reported in Fig. 3 (right), while Fig. 4 (left) shows the strain gauges located on section 4.0 of the blade (at 4.0 m distance from the clamping). Fig. 4 (right) shows the strain time histories measured by 2 of the 8 sensors placed on section 4.0.

3.2. WT blade FE model

The FE model has been developed by DTU Wind Energy using the commercial software MSC Nastran and afterwards exported to Simcenter 3D for model validation. It consists in a 3D model made up of around 130 000 six-sided layered composite (8 or 20 nodes) elements. At the blade root, a spider connection links the nodes belonging to the circular interface plate to the central node of the root section, which is clamped. The model has been validated using modal parameters estimated via Simcenter Polymax from hammer and shaker tests performed on the blade in free–free conditions [11,73]. Afterwards, the model materials characteristics have been tuned to the specific application by referencing to modal properties determined via Simcenter Polymax using data acquired during hammer tests with the blade in clamped–free conditions, i.e., the same boundary conditions adopted during the pull and release tests. During the considered hammer test, the blade was excited either in the flapwise or edgewise direction and it was instrumented via 64

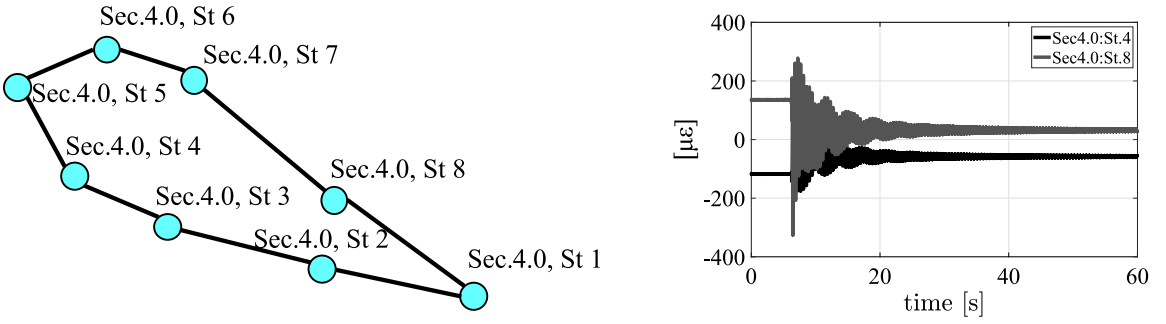

Fig. 4. Sensor locations on section 4.0 (left). Strain responses measured by sensors 4 and 8 on section 4.0 during the pull and release test (right).

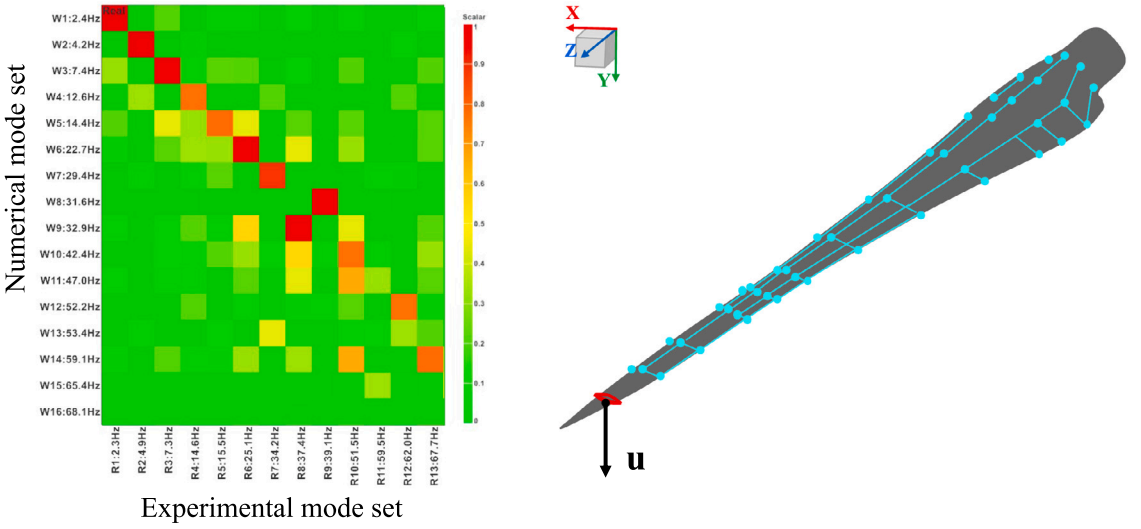

Fig. 5. MAC between numerical and experimental mode shapes from hammer test (left). Test and FE model geometries alignment (right).

accelerometers measuring both X and Y directions (including the driving point one). Sensors were distributed along the blade on 14 sections and only half of the blade surface was covered. Fig. 5 (left) shows the Modal Assurance Criterion (MAC) diagram resulting from the correlation of the FE model mode shapes (computed using NX Nastran SOL103 Real Eigenvalues) and the experimental mode shapes obtained from the described hammer test. Although a good matching between the numerical and experimental mode shapes is globally achieved for the first ten normal modes, i.e., up to 43 Hz, the switching of modes 8 and 9 in the MAC diagram must be highlighted. Modes 8 and 9 comprise a combination of torsion and high-order flap-wise bending. Therefore, the 20% and 13% relative frequency errors, respectively associated to mode 8 and 9, could be ascribed to the blade being instrumented only on the top surface during tests. In Bayesian filtering, this type of modeling errors are compensated via the process noise term, which allows for reliable predictions even in presence of model mismatches. A Reduced Order Model (ROM) of the blade has been built following the procedure outlined in Section 2 in order to reduce the computational effort derived from the high dimensionality of the original FE model. The ROM reduction basis has been built taking into account the first ten modes (frequency range of interest: 0–43 Hz) and one residual attachment mode related to the unknown force to be estimated. The considered application point and direction for the unknown input **u** are highlighted in Fig. 5 (right). A visual information regarding the accuracy of the resulting ROM is displayed in Fig. 6 via the comparison between the experimental and the simulated responses in frequency domain for sensors St4 and St8 on section 4.0. The simulated responses have been computed by performing a forward simulation of the model, pre-loaded by the blade weight, with a load time history reconstructed using the available static load scalar value.

4. Results: Input–response estimates

In order to validate the efficacy of the proposed algorithm on the task of input–response prediction, it is common practice to compare estimated signals to the corresponding measured reference. We follow such a procedure here by splitting the set of recorded dynamic response data into a measured and an unmeasured subset. The unmeasured subset refers to the quantities that are to be estimated via use of the proposed scheme. The "virtually sensed" signals are then compared to the reference (measured)

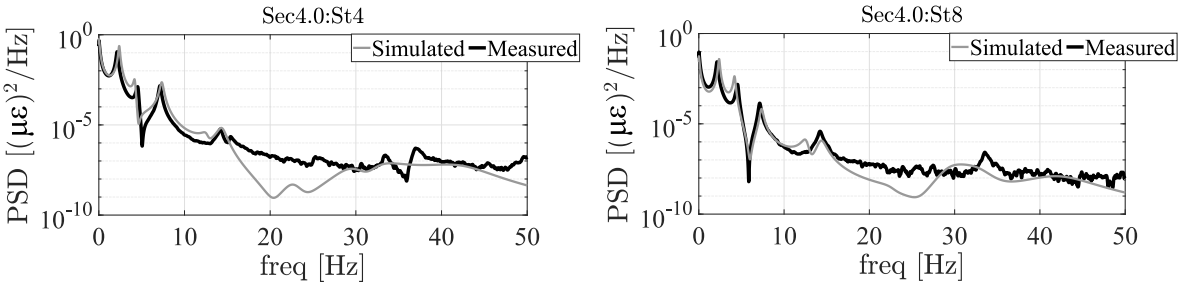

Fig. 6. Power Spectral Density (PSD) of responses measured (solid black line) and simulated (solid gray line) at locations St.4 (Sec4.0), St.8 (Sec4.0).

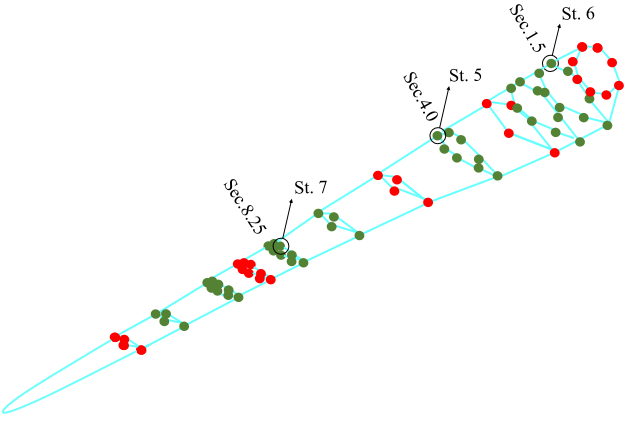

Fig. 7. Sensing configuration: "measured" (red) and "unmeasured" (green) locations.

time histories in order to evaluate the prediction performance. For the hereby analyzed pull and release tests on the research wind turbine blade, the "measured" and "unmeasured" locations were defined by assuming that the blade could only be instrumented at certain sections, due to time constraints and limited sensor availability. The resulting sensing configuration, according to which strain response is acquired at only 28 locations out of the original 76 positions, is reported in Fig. 7. The number of measured responses meets the minimum sensors requirement for CMS-ME described in Section 2.3.1.

4.1. Response prediction through the CMS-ME approach

This Section discusses the prediction results achieved by exploiting the CMS-ME approach proposed in Section 2.3.1. Fig. 8 illustrates the strain response estimation results achieved using the CMS-ME approach (in green) at three "unmeasured" locations according to the sensing configuration reported in Fig. 7. The curves estimated via the CMS-ME approach are compared in Fig. 8 to the experimentally measured time histories (in black) and those estimated using the standard ME technique (in orange). Moreover, Fig. 8 reports in gray the simulated time histories, i.e., the response signals obtained by performing a forward simulation of the model (pre-loaded by the blade weight) for the given loading history. During the analyzed pull and release tests, only the scalar value of the static force applied right before the blade release instant was acquired. Therefore, an artificial input time history has been reconstructed using this information for obtaining the simulated free-vibrations shown in gray in Fig. 8.

Fig. 8 reports a good agreement between the experimentally measured time histories (in black) and those estimated using ME (in orange) and CMS-ME (in green) at the corresponding locations. Moreover, the results confirm that the process of expanding measured quantities to unmeasured locations through a modal basis allows to correct modeling errors, as indicated by the discrepancy delivered purely via use of the simulation model. From the time histories and PSDs comparison, quite a high mismatch can be observed between the measured and the simulated signals due to approximations in modeling damping. To the contrary, the curves estimated via standard ME technique and our CMS-ME approach are not affected by this error, since the methods exploit ME from sparse measurements; a step which delivers a correction of the response in the unmeasured locations. The analysis of the strain response time histories highlights the slightly better performance of the CMS-ME method with respect to the standard ME approach. Indeed, the strain response PSDs reveal that the CMS-ME estimates have a better agreement with the experimental strain responses in frequency domain, e.g. PSD at location Sec8.25:St7 between 7 and 15 Hz. For extending the validity of the characteristic results reported in Fig. 8 to all the "unmeasured" locations along the blade, an overview of the strain estimation results obtained through the ME and CMS-ME approaches is offered in Figs. 9 and 10. The plots in Figs. 9 and 10 quantify the global prediction accuracy, respectively, in time and frequency domain by making use of two quality indicators.

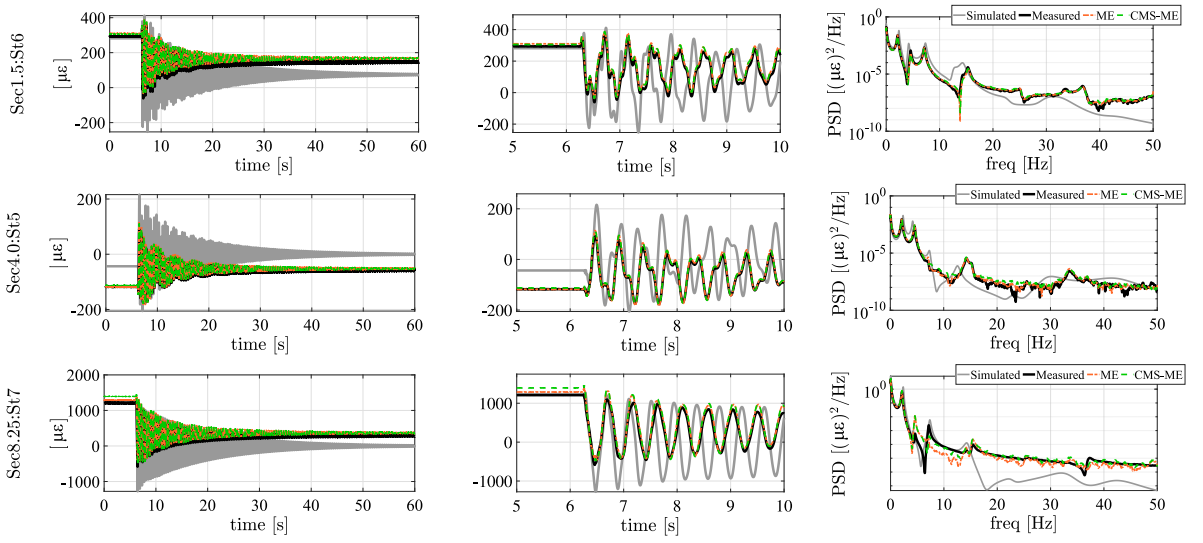

Fig. 8. Time history (left), detailed time history (middle) and PSD (right) of responses of strain sensors St.6 (Sec1.5), St.5 (Sec4.0) and St. 7 (Sec. 8.25). Measured and simulated signals are respectively shown by a solid black line and a solid gray line, while those estimated via ME and CMS-ME are respectively denoted via a dashed orange line and a dashed green line.

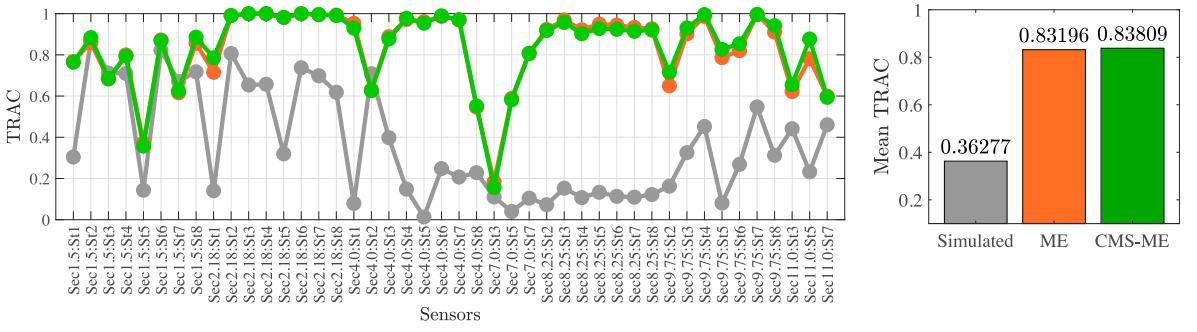

Fig. 9. TRAC values for the simulated strain responses (gray line), the ME (orange line) and CMS-ME (green line) strain response predictions at "unmeasured" locations according to the adopted sensing configuration (left). Mean TRAC values for the simulated strain responses (gray), the ME (orange) and CMS-ME (green) strain response predictions at "unmeasured" locations (right).

The quality indicator adopted to compare the results of the predicted and measured signals in time domain is the so-called Time Response Assurance Criterion (TRAC). The TRAC formulation is reported in Eq. (33), where $\hat{\mathbf{z}}^p$ is the vector of the predicted time histories at the "unmeasured" locations and $\mathbf{z}^p$ contains the corresponding actual responses acquired by physical sensors. In Eq. (33), the explicit dependency with respect to time of the signals is omitted.

$$TRAC = \frac{[\mathbf{z}^{p^T}\hat{\mathbf{z}}^p]^2}{[\hat{\mathbf{z}}^{p^T}\hat{\mathbf{z}}^p][\mathbf{z}^{p^T}\mathbf{z}^p]} \tag{33}$$

The TRAC quantifies the correlation between the predicted and the measured time histories for a single DOF for a chosen response window. For the analyzed case study, the entire time length of the recorded signals has been used for the TRAC computation. When a good correlation between the measured time signal at a certain location and its corresponding estimated time history is achieved, the TRAC assumes values close to 1. A value that is close to 0, indicates therefore poor estimation accuracy. Fig. 9 (left) compares the TRAC values for the simulated strain responses (in gray) and the ME (in orange) and CMS-ME (in green) predictions at the "unmeasured" locations ordered from the blade root (left) to the blade tip (right). Fig. 9 (right) reports the TRAC value averaged over the entire set of predicted strain signals for the three cases hereby taken into account. Both the TRAC trend and the low averaged TRAC value for the simulated responses confirm the inaccuracy delivered via the simulation model. Fig. 9 (left) shows that a TRAC value higher than 0.6 is achieved via both the ME and the CMS-ME approach for the 88% of the estimated quantities and higher than 0.8 for the 70%. The low TRAC appearing for sensors close to the blade root, i.e., Section 1.5, can be due to possible errors in the ME and CMS-ME bases due to BC uncertainties.

The so-called Frequency Response Assurance Criterion (FRAC) reported in Eq. (34) has been adopted in this work to compare the predicted and the measured signals in frequency domain. Similarly to the TRAC, the FRAC quantifies the correlation for one DOF

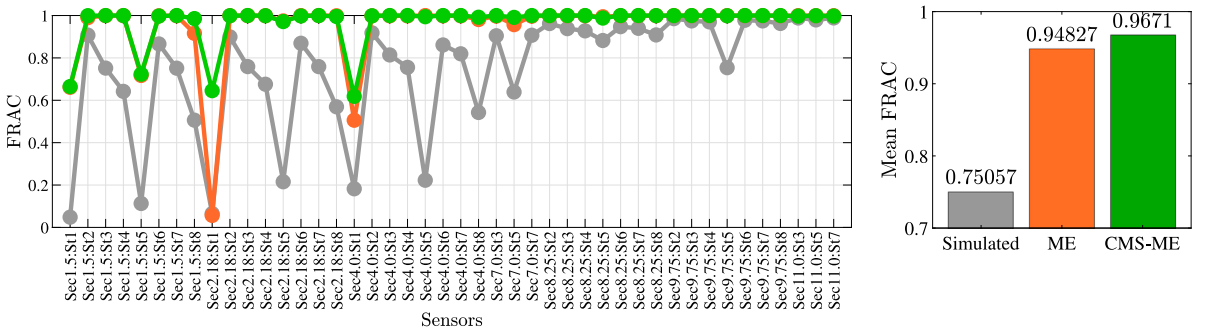

Fig. 10. FRAC values for the simulated strain responses (gray line), the ME (orange line) and CMS-ME (green line) strain response predictions at "unmeasured" locations according to the adopted sensing configuration (left). Mean FRAC values for the simulated strain responses (gray), the ME (orange) and CMS-ME (green) strain response predictions at "unmeasured" locations (right).

between the estimated $\hat{\mathbf{Z}}^p$ and the measured $\mathbf{Z}^p$ frequency domain signals for the chosen frequency range. In Eq. (34), the explicit dependency with respect to frequency of the signals is omitted.

$$FRAC = \frac{[\mathbf{Z}^{p^T}\hat{\mathbf{Z}}^p]^2}{[\hat{\mathbf{Z}}^{p^T}\hat{\mathbf{Z}}^p][\mathbf{Z}^{p^T}\mathbf{Z}^p]} \tag{34}$$

The mean FRAC (Fig. 10 (right)) and the FRAC trend along the blade (Fig. 10 (left)) confirm the potential of both the ME-based approaches to deliver accurate frequency domain predictions in the chosen bandwidth (0–50 Hz). Moreover, the discrepancy between the simulated and measured frequency domain signals encountered in the PSDs plots in Fig. 8 is clearly highlighted in Fig. 10.

From the global comparison provided in Figs. 9 (right) and 10 (right), it can be concluded that the CMS-ME approach outperforms – on average – the standard ME method. Despite the valuable response predictions achieved via the CMS-ME approach, the focus of this work lies in the Bayesian filtering context with the intent to exploit the ability of Bayesian estimators to better account for model and measurement errors. Additionally, specific filters, e.g. the AKF, can be adopted for joint input-state estimation, thus allowing to simultaneously address response prediction and inverse load identification from sparse response measurements. Nevertheless, the presented results suggest that the CMS-ME estimations can be adopted as reference for prediction inaccuracy computation within the framework proposed in Section 2.3.

4.2. Input–response estimation through the augmented Kalman filter

This Section treats the use of the AKF for input-state estimation during the pull and release tests described in Section 3.1. The results presented in this Section will serve as a reference for evaluating the A-AKF performance. The AKF time-invariant $\mathbf{Q}^a$ matrix is conventionally chosen by setting q^{n_d} and q^{n_v} to very low numbers respectively compared to the order of magnitude of the displacements and velocities within the state vector and selecting q^u by means of the L-curve metric. The diagonal entries of $\mathbf{R}$ can be instead set basing on the noise recorded by the relative measurement channels. For this application, an order of magnitude of $10^{-2}uE^2$ has been computed and used for all the $\mathbf{R}$ matrix diagonal entries. The initial condition, $\hat{x}_0^a$, of the augmented state vector contains the information regarding the pre-deformation of the blade under its weight.

In Fig. 11 the L-curve is presented, where the smoothing and error norms trend is shown for several values of q^u. The smoothing norm is defined as:

$$\sum_{k=1}^{n} \|\hat{\mathbf{u}}_k\|_2^2 \tag{35}$$

where n is the total number of time steps and $\mathbf{u}_k$ is the vector of estimated inputs at the specific point in time k. The error norm is instead related to the measured responses and it is expressed by:

$$\sum_{k=1}^{n} \|\mathbf{y}_k^o - \mathbf{H}_o^a \hat{\mathbf{x}}_k^{a+}\|_2^2. \tag{36}$$

It is observed that the plot shown in Fig. 11 does not appear like a perfect L-shape. However, the curve trend for the analyzed experimental case study can be easily interpreted by the user and q^u can be selected at $10^9 N^2$ for the joint input-state estimation via the AKF. For the sake of conciseness, the measurement unit for the covariance matrices will be omitted in the following subsections.

A parametric study regarding the AKF prediction accuracy variation with the selected input process noise covariance is hereby presented. The study has been conducted by analyzing the evolution of response and input estimates quality indicators when q^u varies on a logarithmic uniformly distributed scale. For simplicity, a variable Q can be defined as $q^u = 10^Q$. The TRAC and FRAC indicators have been adopted for response estimation, while the static error SE and the standard deviation SD have been used for input prediction evaluation. The static error is formulated as the difference between the actual static input ($3.17kN$ before the

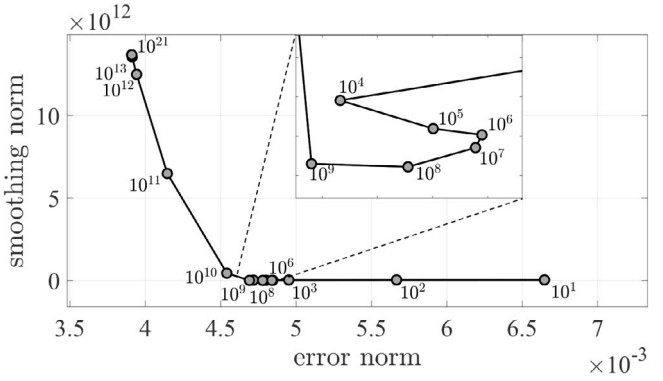

Fig. 11. The L-curve for the joint input-state estimation of the WT blade during pull and release tests using the AKF. Values for q^a are reported on the figure.

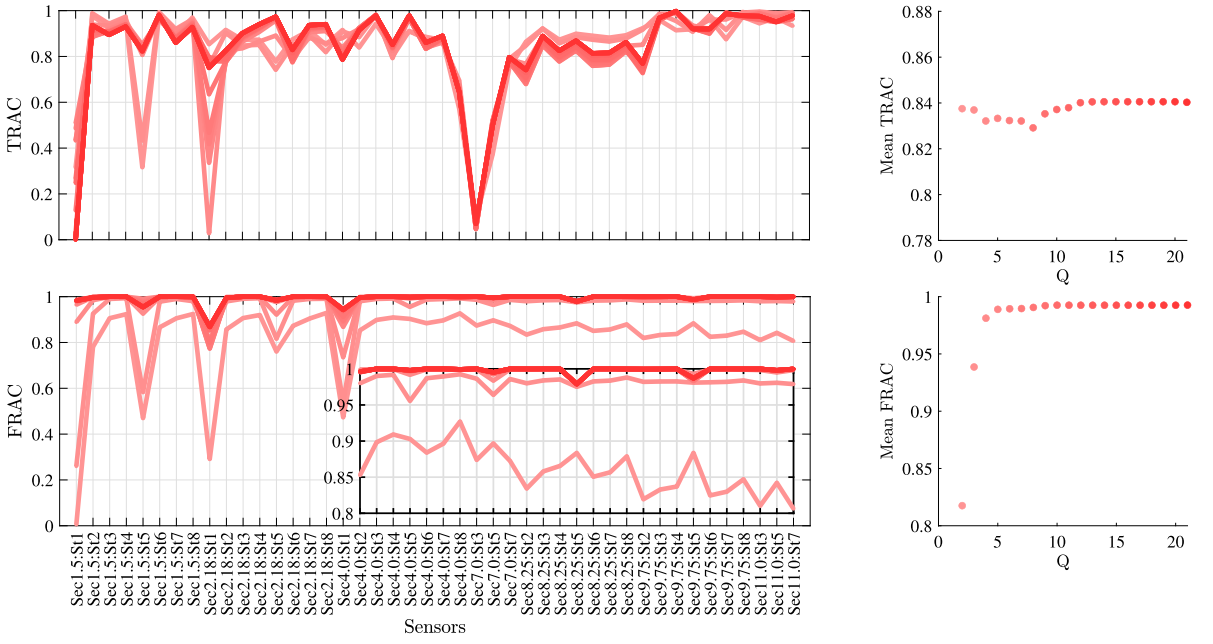

Fig. 12. AKF TRAC trend (top, left) and mean TRAC (top, right) values with increasing Q. AKF FRAC trend and detailed AKF FRAC trend from location Sec4.0:St2 to Sec11.0:St7 (bottom, left). Mean FRAC values with increasing Q (bottom, right).

blade release and $0N$ afterwards) and the mean value of the estimated input profile. The standard deviation, instead, quantifies the oscillations that affect the estimated time history after the blade release. Fig. 12 displays the evolution of the AKF response estimation accuracy for Q varying from 2 to 21 with a 1-step increase. In particular, the evolution with Q of the TRAC and FRAC trends along the blade, i.e., their values at "unmeasured" locations ordered from the blade root (left) to the blade tip (right), is reported in Fig. 12 (left). Fig. 12 (right) displays instead the values, for the several Q choices, of the TRAC and FRAC indicators averaged over the entire set of predicted responses. The entire time length of the recorded signals has been adopted for the TRAC computation, while the frequency range 0–50 Hz has been used for calculating the FRAC values. The analysis of the TRAC and FRAC trends with Q highlights that the most reliable response predictions are achieved for $Q \geq 10$.

While response estimates are not strongly affected by the variation of Q above $Q = 10$, the input prediction accuracy is instead highly dependent on Q, as depicted in Fig. 13 via the SE and SD trends. According to the latter, values of Q that optimize response estimation ($Q \geq 10$) generate high input prediction inaccuracy. Moreover, the minimization of SE is achieved for $Q = 4$, while the value which minimizes SD is $Q = 7$. This behavior demonstrates that there is no level of Q able to provide both the lowest amount of oscillations and the minimal static error. Fig. 13 also shows that the Q value identified via the L-curve ($Q = 9$) produces SE and SD levels which are higher then the achievable minima. Therefore, the SD and SE evolution reported in Fig. 13 proves that the L-curve approach is not optimal for pull and release type of data sets.

Fig. 14 shows a comparison between the input time histories estimated via the AKF with $Q = 4$ (value which allows for SE minimization), $Q = 7$ (value which allows for SD minimization), $Q = 9$ (value identified via the L-curve) and the typical step-type

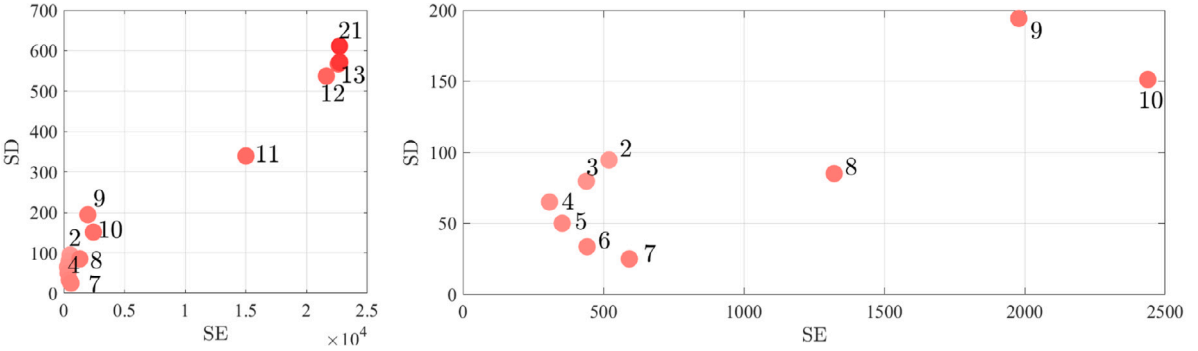

Fig. 13. AKF SE and SD evolution with increasing Q: full (left) and detailed (right) view. Values for Q are reported on the figure.

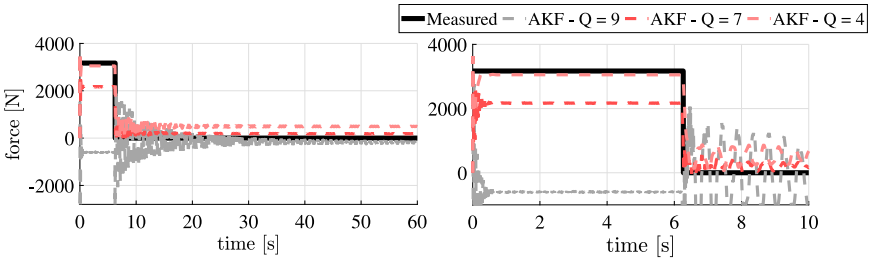

Fig. 14. Input "measured" (black) and estimated time histories (left) and detailed time histories (right) at different levels of Q.

load adopted during pull and release tests. As these tests are taken in an output-only fashion, only the scalar value of the static force applied right before the blade release is available from test data. The "measured" curve proposed in Fig. 14 has been artificially reconstructed using this information, with the purpose of validating the achieved load predictions. Therefore, it is worth noting that the actual load applied during the test may be slightly deviating from the black curve reported in Fig. 14.

The input time histories reported in Fig. 14 reflect the SE and SD trends: oscillations are minimal for $Q = 7$, while the static load is better captured by the AKF when $Q = 4$. Moreover, the input process noise covariance identified via the L-curve ($Q = 9$) generates large mismatches between the estimated and the actual load profiles. This result confirms that the L-curve is not suitable for tuning the AKF when applied for input-state estimation during tests with a pull and release type of loading. The latter comprise a constant input which is then abruptly removed and, therefore, deviates from the common random noise loading scenario in which the AKF normally excels. The pull and release load, i.e., a stationary load before and after the release instant, is difficult to be captured by the AKF, which adopts a random-walk model, i.e., a non-stationary model, to represent the unknown input evolution in time. In fact, the random-walk model can be treated as a first order autoregressive process that has a root on the unit circle, which does not satisfy the stationarity condition [28]. As a result, the oscillations and the biased error appearing in the estimated input time history can be reduced by manual tuning but not completely removed, as displayed in Figs. 13 and 14. Despite the inability of the L-curve to provide satisfactory input estimations, the AKF predictions obtained for $Q = 9$ will be adopted as reference for evaluating the performance of the hereby proposed algorithm. Indeed, the Q values which minimize the input errors ($Q = 4$ and $Q = 7$) would generate lower TRAC and FRAC values, i.e., lower response prediction accuracy. Additionally, since the A-AKF approach aims to be a user-independent procedure, reference results should also be obtained with limited manual intervention.

4.3. Input–response estimation through the adaptive-noise augmented Kalman filter

This Section reports on the results obtained by applying the A-AKF described in Section 2.3 for joint input-state estimation during the pull and release tests described in Section 3.1. For assessing the algorithm validity, the sensing configuration shown in Fig. 7 has been adopted. It is worth mentioning that the A-AKF relies on CMS-ME for response estimation. As a consequence, the number of sensors selected for the A-AKF must satisfy the CMS-ME requirement of having at least $n_o = n_r = 11$ measured signals. The fulfillment of this requisite guarantees robust response predictions for the CMS-ME approach and, as a result, for the A-AKF as well. However, a higher amount of sensors such as the one adopted for this case study, can be a benefit in terms of noise suppression and possibility to capture local deformations and high frequency dynamics. In this sense, Optimal Sensor Placement (OSP) procedures constructed for the AKF, e.g. the one proposed in [74,75], could be exploited for determining the optimal number of measurements for the A-AKF starting from the CMS-ME minimum threshold. The employment of such methodologies would help in guaranteeing both accurate load and response predictions. In order to apply the newly proposed algorithm for the pull and release data set, broad ranges for q^{n_d}, q^{n_v} and q^u have been selected as follows: $q^{n_d}_{min} = q^{n_v}_{min} = q^u_{min} = 10^{-20}$, $q^{n_d}_{max} = q^{n_v}_{max} = q^u_{max} = 10^{20}$. The prediction

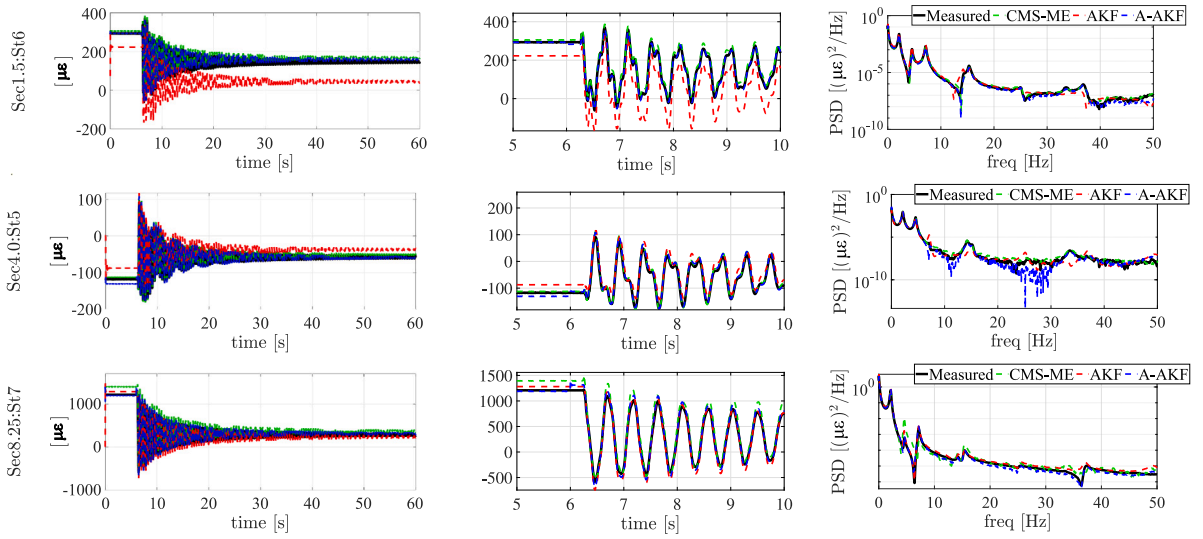

Fig. 15. Time history (left), detailed time history (middle) and PSD (right) of strain response for sensors St.6 (Sec1.5), St.5 (Sec4.0) and St. 7 (Sec. 8.25). Measured signals are indicated via a solid black line. Signals estimated via CMS-ME are indicated in a dashed green line, signals obtained via the conventional AKF in a dashed red line, while those predicted via the A-AKF are denoted via a dashed blue line.

results described in this Section have been obtained via the A-AKF with a $N = 100$ time-steps time window. Two parametric studies regarding the variability of the estimation accuracy with, respectively, the dimension of the window length and the selected ranges bounds adopted for the A-AKF will be presented in Sections 4.3.3 and 4.3.4. This Section also proposes a comparison between the prediction results achieved adopting the A-AKF and those obtained via the AKF when q^u is selected by means of the L-curve metric. Similarly to the AKF settings, the diagonal entries of $\mathbf{R}$ have been set to 10^{-2} for the A-AKF. To the contrary, the A-AKF initialization is performed differently from the AKF: while the AKF initial condition only contains the pre-deformation due to the gravity load, the A-AKF adopts the CMS-ME estimates to define the initial condition. The latter is therefore more accurate since it already contains information about the static response of the blade under the applied unknown load.

4.3.1. Response estimation

Fig. 15 shows the time histories and the related frequency content of the blade response at the three locations pointed out in Fig. 7. A comparison between the signals estimated via CMS-ME, the conventional AKF and the ones obtained by using the proposed A-AKF scheme is offered. Moreover, the estimated curves are compared to the experimentally measured responses at the corresponding locations to prove the algorithm validity.

A global comparison between the conventional approach and the herein proposed procedure, in terms of response estimation accuracy, is shown in Figs. 16 and 17, where, respectively, the TRAC and FRAC values at "unmeasured" locations are displayed for the conventional AKF, the A-AKF and the CMS-ME approach. In particular, Figs. 16 (left) and 17 (left) show, respectively, the TRAC and FRAC trends along the blade, i.e., their values at "unmeasured" locations ordered from the blade root (left) to the blade tip (right). Figs. 16 (right) and 17 (right) display the TRAC and FRAC values averaged over the entire set of predicted responses. The entire time length of the recorded signals has been adopted for the TRAC computation, while the frequency range 0–50 Hz has been used for calculating the FRAC values. Figs. 15, 16 and 17 demonstrate good predictive capabilities for the A-AKF. The time histories reported in Fig. 15 indicate that the A-AKF estimation captures the physical blade response both in the static and the dynamic time frames, while the conventional AKF predictions are affected by higher inaccuracy. Indeed, the AKF response predictions report on average a 25% deviation from the measured value in the static time frame, which is clearly visible in Fig. 15. To the contrary, the A-AKF matches the measured static responses thanks to the more realistic initial conditions determined from the CMS-ME estimates. Fig. 16 confirms the comparison results in time domain: the mean TRAC achieved through the A-AKF overcomes the AKF mean TRAC by providing a TRAC value higher than 0.6 for the 93% of the estimated quantities and higher than 0.8 for the 80%.

Fig. 15 (right) shows that the proposed approach allows to capture the blade response in frequency domain. Moreover, the proposed PSD plots show that the A-AKF estimations follow the frequency content of the physically acquired responses throughout the analyzed frequency bandwidth with good accuracy. However, Fig. 17 (right) reports a 1.43% lower mean FRAC value for the A-AKF with respect to the mean FRAC delivered by the conventional AKF. This trend can be ascribed to the instabilities that the near-online adaptation of the process noise covariance may cause when adopting the A-AKF. Due to this behavior, non-smooth frequency response can appear in certain bandwidths, e.g., PSD at location Sec4.0:St5 between 20 and 30 Hz. Nonetheless, Fig. 15 (right) clearly demonstrates that, outside the limited frequency ranges in which the described effect occurs, the A-AKF predicted spectra match the measured ones with higher accuracy than the signals generated via the conventional AKF regime. Figs. 16 and 17 further show a good agreement between the predictions furnished via the proposed A-AKF algorithm and the reference CMS-ME

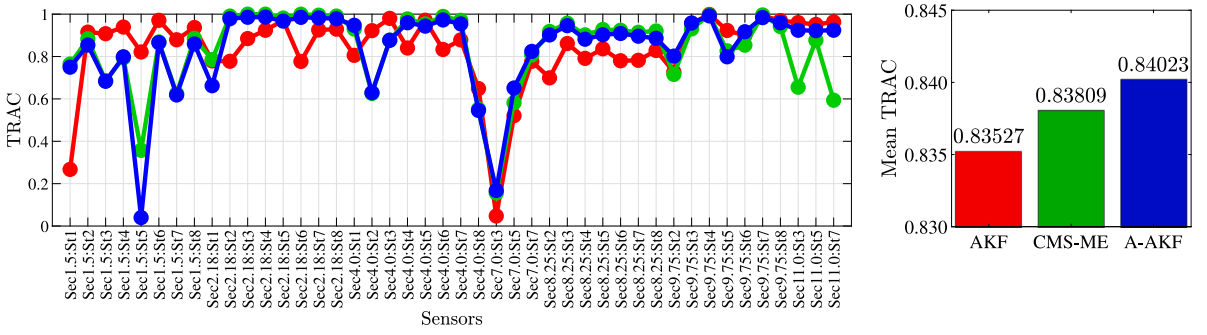

Fig. 16. TRAC values for the CMS-ME (green line), conventional AKF (red line) and A-AKF (blue line) strain response predictions at "unmeasured" locations according to the adopted sensing configuration (left). Mean TRAC values for the CMS-ME (green), conventional AKF (red) and A-AKF (blue) strain response predictions at "unmeasured" locations (right).

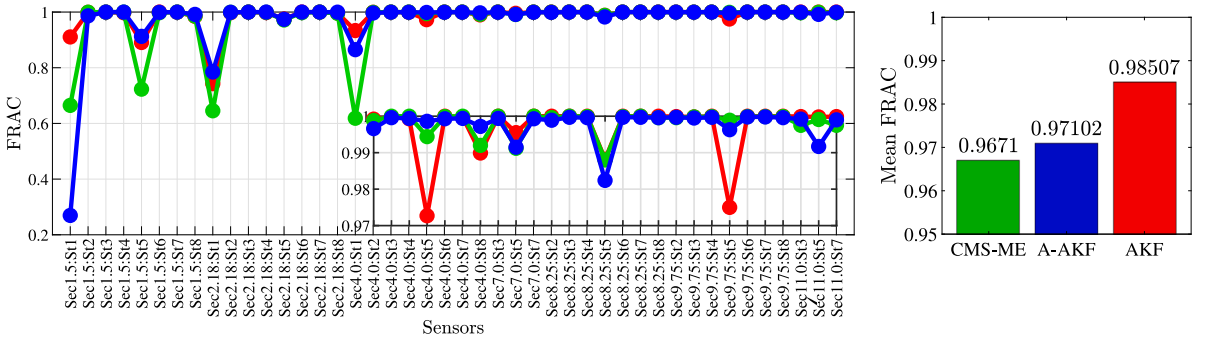

Fig. 17. FRAC values for the CMS-ME (green line), conventional AKF (red line) and A-AKF (blue line) strain response predictions at "unmeasured" locations according to the adopted sensing configuration (left). A detailed view from location Sec4.0:St2 to Sec11:St7 is shown on the plot. Mean FRAC values for the CMS-ME (green), conventional AKF (red) and A-AKF (blue) strain response predictions at "unmeasured" locations (right).

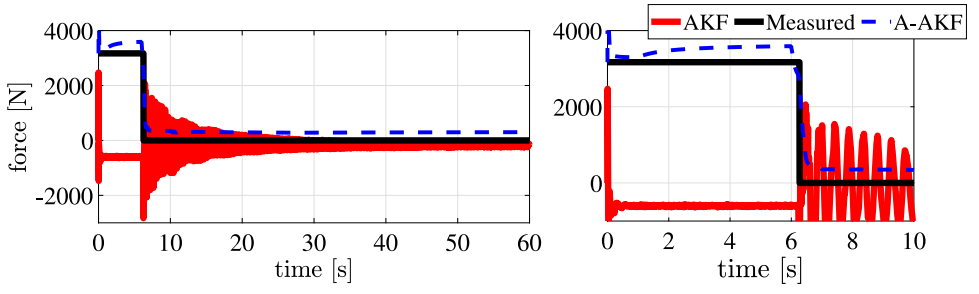

Fig. 18. Input "measured" (black) and estimated (red — AKF, blue — A-AKF) time histories (left) and detailed time histories (right).

method both in time and frequency domains. More specifically, a slightly higher mean TRAC value can be obtained when the A-AKF is adopted with $N = 100$. The superior performance of the proposed algorithm in the frequency domain, i.e., the higher FRAC value reported in Fig. 17 (right), can be visualized by comparing the response PSDs at location Sec8.25:St7 reported in Fig. 15. While the A-AKF predicted signal correctly matches the frequency content of the measured signal in the entire frequency bandwidth, the CMS-ME method overestimates the PSD amplitude around the 4.5 and 15.5 Hz peaks and underestimates it around the 7.2 Hz peak. Moreover, the CMS-ME estimated signal appears highly contaminated by noise at higher frequencies. This behavior confirms that the proposed approach, which draws from the CMS-ME method, simultaneously outperforms it thanks to the higher ability of Bayesian filtering to track measurement and modeling errors by including the noise terms in the system representation.

4.3.2. Input estimation

Fig. 18 shows the input estimation results for the unknown force applied to the blade when the AKF (process noise covariance matrix via the L-curve) and the proposed methodology are adopted.

The two predicted time signals are compared with the reconstructed step-profile followed by the input during the pull and release tests. From the analysis of the time histories reported in Fig. 18, it can be inferred that a good matching between the input predicted

Table 1
Input prediction errors: comparison between the conventional AKF and the A-AKF.

	Conventional AKF	A-AKF
SE	$1978N$	$303N$
SD	$194.25N$	$58N$

via the A-AKF and the actual input profile can be achieved. In particular, both the time instant when the blade is released and the previous static value are identified. To the contrary, when the AKF is used in conjunction with a conventionally selected augmented process noise matrix, the typical pull and release step profile is not detected, i.e., the prediction does not capture the actual input static value and it is affected by high-amplitude oscillations after the blade release. For quantitative comparison purposes, the static error SE and the standard deviation SD are reported in Table 1 for both the AKF and the A-AKF. The major contribution to the A-AKF static error SE is given by the constant offset that affects the A-AKF input profile. Although the blade pre-deformation under its weight is already taken into account, biased errors may be introduced by the assumptions made to model the gravity load, e.g., approximation of the center of gravity position. Hence, part of the gravity load may be estimated together with the external unknown force by the estimators. Moreover, it should be reminded that the unknown input is modeled as a punctual load for VS purposes. This condition only approximates the actual system used to apply the force during tests, i.e., a bungee applied at a certain section. Indeed, the latter generates a distributed load over the section, which could further be affected by fluctuations due to the bungee elasticity. The results listed in Table 1 show that a lower prediction error can be achieved if an automated process noise covariance selection is put in place via the A-AKF. It is important to notice that improved SE and SD indicators can be achieved via the conventional AKF, as presented in Section 4.2 via the parametric study. However, these results would require a substantial manual tuning effort, also implying deterioration of response estimation accuracy.

4.3.3. Parametric study: influence of the time window length

The newly proposed approach for joint input-state estimation relies on the use of a N-steps time window for computing the global prediction error to be minimized within the algorithm. This Section analyzes the influence of the time window length on the estimation accuracy when ranges for q^{n_d}, q^{n_v} and q^u are selected as follows: $q^{n_d}_{min} = q^{n_v}_{min} = q^u_{min} = 10^{-20}$, $q^{n_d}_{max} = q^{n_v}_{max} = q^u_{max} = 10^{20}$.

Fig. 19 shows the evolution of the A-AKF response prediction accuracy for N varying from 10 to 500 with a 10-steps increase. From the analysis of the TRAC trend plot (Fig. 19 (top, left)) it can be inferred that the influence of the chosen time window length is bounded within a narrow range of variation. This behavior is confirmed by Fig. 19 (top, right), which shows that the mean TRAC maintains a value bounded between and 0.80 and 0.86 with increasing N. It can be further noticed that an increasing trend is exhibited for low N values. After this first adaptation phase, the algorithm yields mean TRAC values which exhibit low variability. The evolution of the A-AKF response estimation accuracy in the frequency domain is reported in Fig. 19 by means of the FRAC trend and mean FRAC evolution with increasing N. Similarly to the mean TRAC trend, the mean FRAC shows an initial phase affected by higher variability after which it stabilizes around a value approximately equal to 0.97. From Fig. 19, it can be inferred that the mean FRAC spans an even narrower range ($0.965 - 0.975$) with respect to the mean TRAC.

Fig. 20 displays the variation of the SE and SD input estimation inaccuracy indicator for increasing values of N. The conclusions drawn for the response estimation accuracy can be extended to the input prediction based on Fig. 20; both SE and SD reach their maximum for low N, while stable minimum values for both variables are obtained from a certain N value (between 100 and 150). The last assumption is particularly valid for what concerns the SD indicator. For values higher than $N = 100$, the selection of a broader time window for the A-AKF algorithm does not improve the oscillatory behavior, which results as an artifact in the estimated input profile. It is important to emphasize that the values for which the SE and SD minima are found lie close to the optimal values for which both the mean TRAC and mean FRAC become stable. The conducted parametric study thus demonstrates that a unique choice for N will generate the same effect on the input and response estimation accuracy delivered via the A-AKF. The optimal choice for N should be high enough to surpass regions of algorithmic instability. On the other hand, an exaggerated increase in N would cause the A-AKF to deviate from the near real-time assumption and would not bring any benefit in terms of estimation accuracy. For this reason, N values between 100 and 150 can be considered as optimal. It should be noted that, although a default choice for N in the suggested range would already make the algorithm user-independent, a random N selection could still be put in place. The latter would be justified by the generally limited fluctuations in the prediction accuracy for $10 \leq N \leq 500$. However, such a random selection should still employ a limited time window length in order to ensure near real-time applicability.

4.3.4. Parametric study: influence of q^{n_d}, q^{n_v} and q^u range bounds

The A-AKF requires an a priori selection of the ranges within which q^{n_d}, q^{n_v} and q^u can vary. This Section studies the influence of the covariances range on the overall input and response estimation accuracy when a $N = 100$ time-steps window is adopted. In order to simplify the analysis, the following assumptions are made:

- The ranges are symmetrical, i.e, $q^{n_d}_{min} = -q^{n_d}_{max}$, $q^{n_v}_{min} = -q^{n_v}_{max}$ and $q^u_{min} = -q^u_{max}$.
- The same range is adopted for the three variables q^{n_d}, q^{n_v}, q^u.

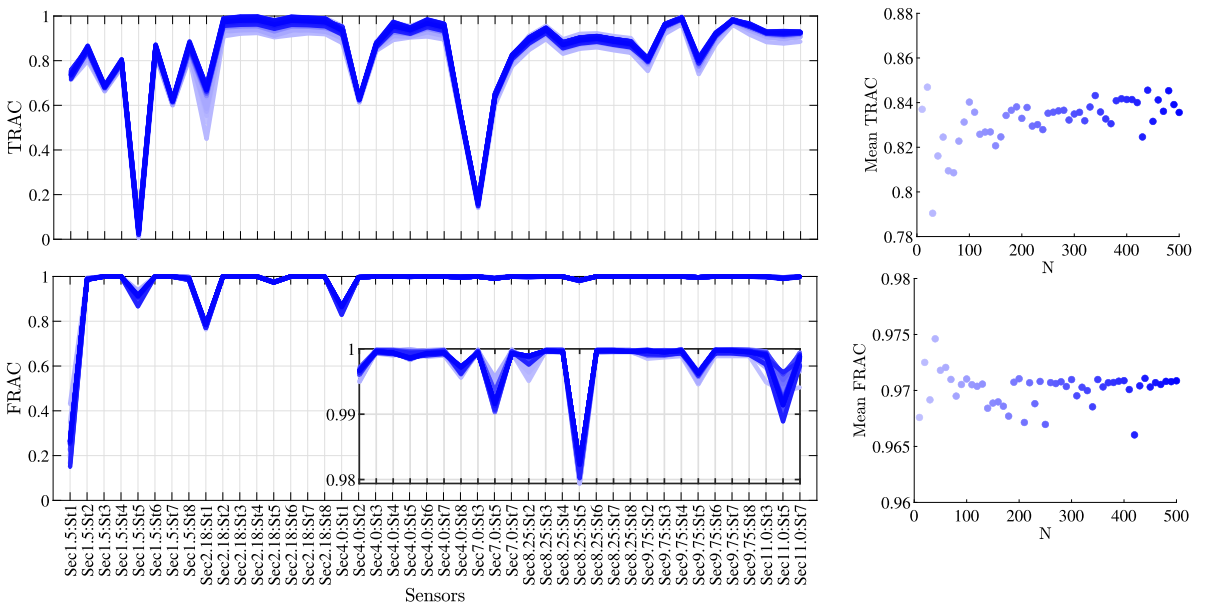

Fig. 19. A-AKF TRAC trend (top, left) and mean TRAC (top, right) values with increasing N. A-AKF FRAC trend and detailed A-AKF FRAC trend from location Sec4.0:St2 to Sec11.0:St7 (bottom, left). Mean FRAC values with increasing N (bottom, right).

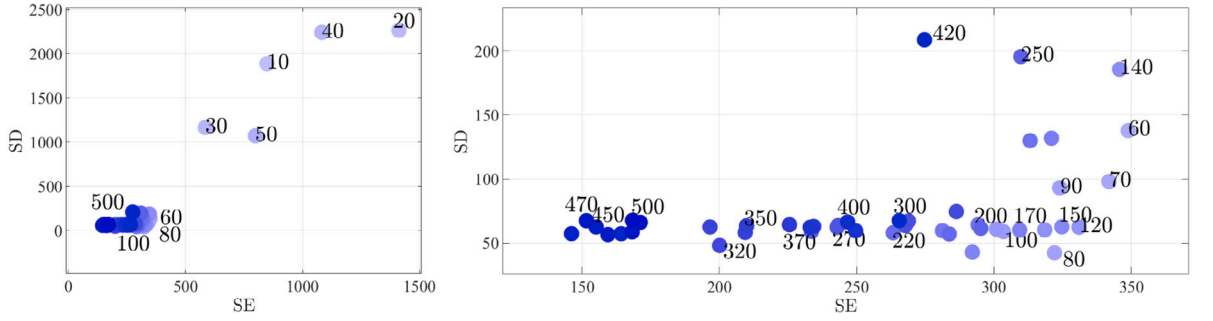

Fig. 20. A-AKF SE and SD evolution with increasing N: full (left) and detailed (right) view. Values for N are reported on the figure.

Therefore, a variable Q can be defined such that: $q^{n_d}_{min} = q^{n_v}_{min} = q^{u}_{min} = 10^{-Q}$ and $q^{n_d}_{max} = q^{n_v}_{max} = q^{u}_{max} = 10^{Q}$

Fig. 21 displays the evolution of the A-AKF response estimation accuracy for Q varying from 2 to 23 with a 1-step increase. The TRAC trend and mean TRAC plots reported in Fig. 21 show that approximately up to a 3% higher response estimation accuracy could be achieved by adopting a very low Q, i.e., by heavily bounding the range of values that q^{n_d}, q^{n_v} and q^{u} could span. For $Q \geq 5$, the TRAC seems to stabilize around a certain value. However, the FRAC and mean FRAC evolution reported in Fig. 21 shows a different behavior: the response estimation accuracy in frequency domain reaches the highest value for $Q = 5$ and remains stable for higher Q.

Fig. 22 displays the variation of the SE and SD input estimation inaccuracy indicators for increasing values of Q. For $2 \leq Q \leq 4$, the SE indicator reaches the lowest values while SD is maximized. This result highlights that for very narrow ranges, the best match between the predicted input mean value and the measured one could be achieved but the estimated time history would be affected by large oscillations, i.e., the predicted input would not be static. For $Q \geq 5$, both SD and SE stabilize, i.e., varying the ranges width would not cause any variation in the input prediction accuracy.

According to Figs. 21 and 22, the same overall estimation accuracy can be achieved for $Q \geq 5$. Although selecting narrow ranges, i.e., $Q \leq 5$, would improve the TRAC and SE estimators, the resulting response error in frequency domain would increase and the predicted input would be affected by large oscillations. The parametric study reported in this Section demonstrates that broad ranges can be set by the user for q^{n_d}, q^{n_v} and q^{u} without affecting the estimation results. Therefore, no particular prior belief on the most suitable ranges for q^{n_d}, q^{n_v} and q^{u} is required for obtaining optimal results via the A-AKF.

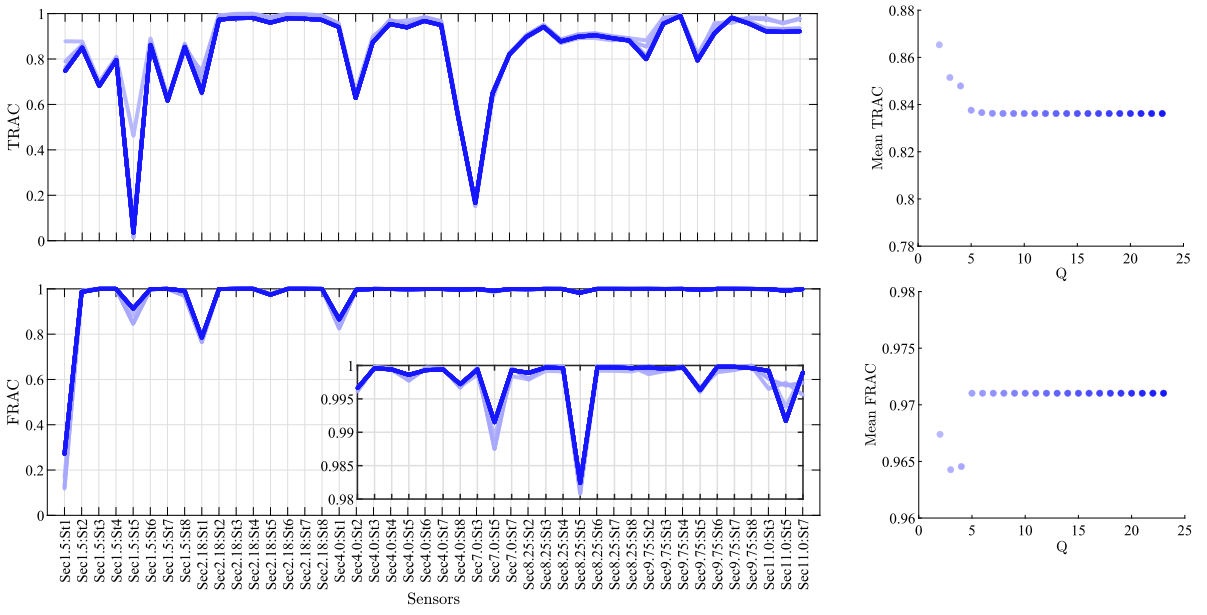

Fig. 21. A-AKF TRAC trend (top, left) and mean TRAC (top, right) values with increasing Q. A-AKF FRAC trend and detailed A-AKF FRAC trend from location Sec4.0:St2 to Sec11.0:St7 (bottom, left). Mean FRAC values with increasing Q (bottom, right).

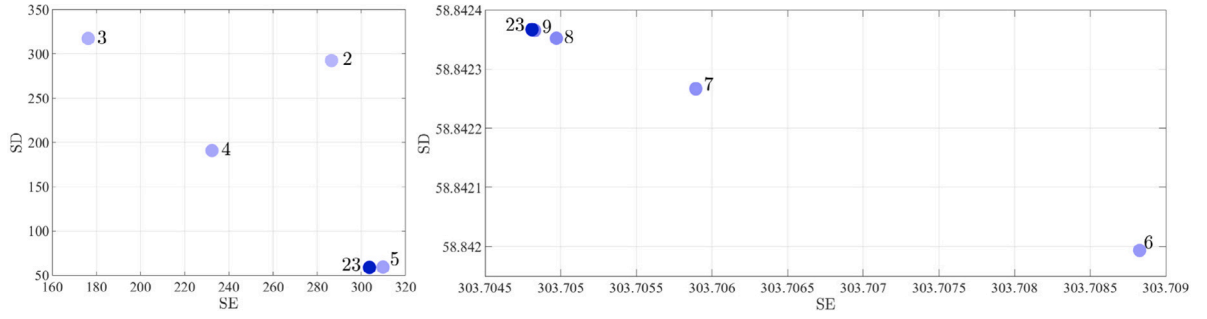

Fig. 22. A-AKF SE and SD evolution with increasing Q: full (left) and detailed (right) view. Values for Q are reported on the figure.

5. Conclusions

In this work, a novel approach has been presented to tackle the problem of adaptive noise calibration for the task of joint input-state estimation via Kalman-type filters. This task is the driving process during VS applications, where typically few sparse response measurements are available and recovery of response and inputs in unmeasured locations is sought. In particular, an automated procedure has been developed for determining the augmented process noise covariance matrix in a near-online fashion when the AKF is adopted for joint input-state estimation. The working principle of the so-called A-AKF developed within this work is based on the assumption of a time-variant diagonal augmented process noise covariance matrix, in which both the terms related to the states and the input assume the role of regularization parameters. The developed approach relies on the minimization of the input and response prediction errors. The first is based on the error covariance matrix term associated to the unknown input, while the latter relies on the acquired signals for the measured quantities and on predictions achieved via the CMS-ME method for the unmeasured ones. The proposed methodology has been tested for loads (input) and full-field response prediction during the so-called pull and release experimental tests on a full-scale research WT blade. In order to reduce the computational effort due to the high dimensionality of the blade FE model, a ROM has been derived from an experimentally validated FE model using a CMS technique.

The results indicate that the A-AKF provides accurate response predictions without the need for offline user-dependent selection of the covariance matrix associated to model uncertainties, which forms a well-known limitation of the conventional AKF. A parametric study has demonstrated that the A-AKF response prediction accuracy outperforms both the conventional AKF and the CMS-ME methods, provided that a sufficiently large time window is adopted for the algorithm. To what concerns the input, large errors are encountered when a conventional augmented process noise covariance matrix is adopted, with the input-related covariance term

assigned via the classical L-curve approach. As demonstrated via the presented parametric study, these errors could be minimized via a substantial manual tuning. Besides the need of user intervention, the tuning procedure has proven not to be able to simultaneously minimize both the oscillations and the static error. Additionally, minimized AKF input errors would lead to deterioration of response estimation accuracy. When the process noise covariance matrix is tuned via the L-curve, the AKF is not able to capture the actual input profile (corresponding to a step) and large oscillations are affecting the estimated signal following blade release. To the contrary, by adopting the A-AKF, the predicted input profile matches the actual experimental load and the static error, as well as the standard deviation of the oscillations following release, are minimized. The same behavior for different adopted time window lengths can be observed for the input. Moreover, the input inaccuracy indicators are minimized for the same time window dimension which maximizes the response performance both in time and frequency domains. It should be noted that the variability in performance as a result of the chosen window length is sufficiently limited to justify a random selection of the latter, which should though comprise narrow ranges in order to guarantee a near-online procedure. Under these latter assumptions, the A-AKF can be considered as a user-independent method for joint input-state estimation in near real-time. The latter statement is confirmed by the proved independence of the overall A-AKF estimation accuracy from the selected covariance ranges. The parametric study with respect to the ranges bounds has proven that no prior knowledge regarding the most suitable ranges width is needed in order to guarantee the A-AKF optimal performance. Further investigations will focus on testing the A-AKF on different structures and for different type of excitation signals. Depending on the observed outcome, a library of prediction inaccuracy indicators to be used in the algorithm may be developed in order to cover several hypothetical scenarios.

Declaration of competing interest

The authors declare that they have no known competing financial interests or personal relationships that could have appeared to influence the work reported in this paper.

Data availability

The authors do not have permission to share data.

Acknowledgments

The authors gratefully acknowledge the European Commission for its support of the Marie Sklodowska Curie program through the ITN DyVirt project (GA 764547).

The authors would like to extend their gratitude to the DTU Wind Energy department for providing the blade FE model and relevant experimental data, developed in the framework of the project "BLATIGUE: Fast and efficient fatigue test of large wind turbine blades", supported by the Danish Energy Agency through the Energy Technology Development and Demonstration Program (EUDP), Grant No. 64016-0023.

The authors would like to also acknowledge the project "RELIABLADE: Improving Blade Reliability through Application of Digital Twins over Entire Life Cycle", supported by the Danish Energy Agency through the Energy Technology Development and Demonstration Program (EUDP), Grant No. 64018-0068, the support of which is greatly appreciated.

References

[1] Keith Worden, EJ Cross, P Gardner, RJ Barthorpe, DJ Wagg, On digital twins, mirrors and virtualisations, in: Model Validation and Uncertainty Quantification, Volume 3, Springer, 2020, pp. 285–295.
[2] F Sayer, A Antoniou, S Goutianos, I Gebauer, K Branner, C Balzani, ReliaBlade project: A material's perspective towards the digitalization of wind turbine rotor blades, IOP Conf. Ser.: Mater. Sci. Eng. 942 (1) (2020) 012006.
[3] International Electrotechnical Commission, et al., International standard iec 61400-23 Wind turbine generator systems–part 23: full-scale structural testing of rotor blades, in: Wind Turbines-Part, Vol. 1, 2014.
[4] Hak Gu Lee, Jisang Park, Static test until structural collapse after fatigue testing of a full-scale wind turbine blade, Compos. Struct. 136 (2016) 251–257.
[5] Jinshui Yang, Chaoyi Peng, Jiayu Xiao, Jingcheng Zeng, Suli Xing, Jiaotong Jin, Hang Deng, Structural investigation of composite wind turbine blade considering structural collapse in full-scale static tests, Compos. Struct. 97 (2013) 15–29.
[6] Peter R Greaves, Robert G Dominy, Grant L Ingram, Hui Long, Richard Court, Evaluation of dual-axis fatigue testing of large wind turbine blades, Proc. Inst. Mech. Eng. Part C: J. Mech. Eng. Sci. 226 (7) (2012) 1693–1704.
[7] Oscar Castro, Federico Belloni, Mathias Stolpe, Süleyman Cem Yeniceli, Peter Berring, Kim Branner, Optimized method for multi-axial fatigue testing of wind turbine blades, Compos. Struct. 257 (2021) 113358.
[8] Xiao Chen, Sergei Semenov, Malcolm McGugan, Steen Hjelm Madsen, Süleyman Cem Yeniceli, Peter Berring, Kim Branner, Fatigue testing of a 14.3 m composite blade embedded with artificial defects–damage growth and structural health monitoring, Composites A 140 (2021) 106189.
[9] Othman Al-Khudairi, Homayoun Hadavinia, Christian Little, Gavin Gillmore, Peter Greaves, Kirsten Dyer, Full-scale fatigue testing of a wind turbine blade in flapwise direction and examining the effect of crack propagation on the blade performance, Materials 10 (10) (2017) 1152.
[10] Kari Williamson, Push and pull – testing wind turbine blades, Reinf. Plast. 56 (1) (2012) 26–32.
[11] M.M. Luczak, B. Peeters, S. Manzato, E. Di Lorenzo, K. Reck-Nielsen, P. Berring, P.U. Haselbach, K. Branner, Research sized wind turbine blade modal tests: comparison of the impact excitation with shaker excitation, J. Phys. Conf. Ser. 1102 (2018) 012022.
[12] Marcin Luczak, Simone Manzato, Bart Peeters, Kim Branner, Peter Berring, Maciej Kahsin, Dynamic investigation of twist-bend coupling in a wind turbine blade, J. Theoret. Appl. Mech. 49 (3) (2011) 765–789.
[13] Peter Berring, Kim Branner, Christian Berggreen, Henrik W Knudsen, Torsional performance of wind turbine blades-Part 1: Experimental investigation, in: 16th International Conference on Composite Materials, Vol. 43, 2007.

[14] D. Todd Griffith, Thomas G. Carne, Experimental modal analysis of 9-meter research-sized wind turbine blades, in: Structural Dynamics and Renewable Energy, Volume 1, Springer, 2011, pp. 1–14.
[15] Sarah Reese, Daniel Todd Griffith, Miguel Casias, Todd William Simmermacher, Gregory A Smith, Modal testing of the TX-100 wind turbine blade, Technical report, Sandia National Laboratories, 2006.
[16] G.C. Larsen, M.H. Hansen, A. Baumgart, I. Carlen, Modal Analysis of Wind Turbine Blades (Risø-R-1181 (EN)), Roskilde: Riso National Laboratory, 2002.
[17] E. Di Lorenzo, S. Manzato, B. Peeters, V. Ruffini, P. Berring, P.U. Haselbach, K. Branner, M.M. Luczak, Modal analysis of wind turbine blades with different test setup configurations, in: Michael L. Mains, Brandon J. Dilworth (Eds.), Topics in Modal Analysis & Testing, Volume 8, Springer International Publishing, Cham, 2020, pp. 143–152.
[18] E di Lorenzo, S Manzato, Marcin Luczak, B Peeters, Kim Branner, Strain-based operational modal analysis for wind turbine blades, in: 8th International Operational Modal Analysis Conference, IOMAC, 2019.
[19] C. Grinderslev, F. Belloni, S.G. Horcas, N.N. Sørensen, Investigations of aerodynamic drag forces during structural blade testing using high-fidelity fluid–structure interaction, Wind Energy Sci. 5 (2) (2020) 543–560.
[20] J. Kullaa, Bayesian virtual sensing in structural dynamics, Mech. Syst. Signal Process. 115 (2019) 497–513.
[21] Jyrki Kullaa, Virtual sensing of structural vibrations using dynamic substructuring, Mech. Syst. Signal Process. 79 (2016) 203–224.
[22] Peter Avitabile, Model reduction and model expansion and their applications–part 1 theory, in: Proceedings of the Twenty-Third International Modal Analysis Conference, Orlando, FL, USA, 2005.
[23] Peter Avitabile, Pawan Pingle, Prediction of full field dynamic strain from limited sets of measured data, Shock Vib. 19 (5) (2012) 765–785.
[24] Tulay Ercan, Costas Papadimitriou, Optimal sensor placement for reliable virtual sensing using modal expansion and information theory, Sensors 21 (10) (2021).
[25] Alexandros Iliopoulos, Rasoul Shirzadeh, Wout Weijtjens, Patrick Guillaume, Danny Van Hemelrijck, Christof Devriendt, A modal decomposition and expansion approach for prediction of dynamic responses on a monopile offshore wind turbine using a limited number of vibration sensors, Mech. Syst. Signal Process. 68 (2016) 84–104.
[26] Marius Tarp, Bruna Nabuco, Christos Georgakis, Rune Brincker, Expansion of experimental mode shape from operational modal analysis and virtual sensing for fatigue analysis using the modal expansion method, Int. J. Fatigue 130 (2020) 105280.
[27] Kristof Maes, A Iliopoulos, W Weijtjens, C Devriendt, Geert Lombaert, Dynamic strain estimation for fatigue assessment of an offshore monopile wind turbine using filtering and modal expansion algorithms, Mech. Syst. Signal Process. 76 (2016) 592–611.
[28] Vasilis K Dertimanis, EN Chatzi, S Eftekhar Azam, Costas Papadimitriou, Input-state-parameter estimation of structural systems from limited output information, Mech. Syst. Signal Process. 126 (2019) 711–746.
[29] Costas Papadimitriou, Claus-Peter Fritzen, Peter Kraemer, Evangelos Ntotsios, Fatigue predictions in entire body of metallic structures from a limited number of vibration sensors using Kalman filtering, Struct. Control Health Monit. 18 (5) (2011) 554–573.
[30] K.E. Tatsis, V.K. Dertimanis, C. Papadimitriou, E. Lourens, E.N. Chatzi, A general substructure-based framework for input-state estimation using limited output measurements, Mech. Syst. Signal Process. 150 (2021) 107223.
[31] Konstantinos Tatsis, Vasilis Dertimanis, Eleni Chatzi, Response prediction of systems experiencing operational and environmental variability, in: Computing in Civil Engineering 2019: Smart Cities, Sustainability, and Resilience, American Society of Civil Engineers Reston, VA, 2019, pp. 468–474.
[32] Konstantinos E. Tatsis, Vasilis K. Dertimanis, Eleni N. Chatzi, Adaptive process and measurement noise identification for recursive Bayesian estimation, in: Model Validation and Uncertainty Quantification, Volume 3, Springer, 2020, pp. 361–364.
[33] R. Cumbo, T. Tamarozzi, K. Janssens, W. Desmet, Kalman-based load identification and full-field estimation analysis on industrial test case, Mech. Syst. Signal Process. 117 (2019) 771–785.
[34] Enrico Risaliti, Tommaso Tamarozzi, Martijn Vermaut, Bram Cornelis, Wim Desmet, Multibody model based estimation of multiple loads and strain field on a vehicle suspension system, Mech. Syst. Signal Process. 123 (2019) 1–25.
[35] Eleni N. Chatzi, Andrew W. Smyth, The unscented Kalman filter and particle filter methods for nonlinear structural system identification with non-collocated heterogeneous sensing, in: Structural Control and Health Monitoring: The Official Journal of the International Association for Structural Control and Monitoring and of the European Association for the Control of Structures, Vol. 16, (1) Wiley Online Library, 2009, pp. 99–123.
[36] Stefano Mariani, Aldo Ghisi, Unscented Kalman filtering for nonlinear structural dynamics, Nonlinear Dynam. 49 (1) (2007) 131–150.
[37] Konstantinos Tatsis, Long Wu, Paolo Tiso, Eleni Chatzi, State estimation of geometrically non-linear systems using reduced-order models, in: Life Cycle Analysis and Assessment in Civil Engineering: Towards An Integrated Vision, CRC Press, 2018, pp. 219–227.
[38] E Lourens, Edwin Reynders, Guido De Roeck, Geert Degrande, Geert Lombaert, An augmented Kalman filter for force identification in structural dynamics, Mech. Syst. Signal Process. 27 (2012) 446–460.
[39] Frank Naets, Javier Cuadrado, Wim Desmet, Stable force identification in structural dynamics using Kalman filtering and dummy-measurements, Mech. Syst. Signal Process. 50 (2015) 235–248.
[40] Saeed Eftekhar Azam, Eleni Chatzi, Costas Papadimitriou, A dual Kalman filter approach for state estimation via output-only acceleration measurements, Mech. Syst. Signal Process. 60 (2015) 866–886.
[41] Saeed Eftekhar Azam, Eleni Chatzi, Costas Papadimitriou, Andrew Smyth, Experimental validation of the Kalman-type filters for online and real-time state and input estimation, J. Vib. Control 23 (15) (2017) 2494–2519.
[42] Simon J. Julier, Jeffrey K. Uhlmann, Hugh F. Durrant-Whyte, A new approach for filtering nonlinear systems, in: Proceedings of 1995 American Control Conference-ACC'95, Vol. 3, IEEE, 1995, pp. 1628–1632.
[43] Simon J. Julier, Jeffrey K. Uhlmann, New extension of the Kalman filter to nonlinear systems, in: Signal Processing, Sensor Fusion, and Target Recognition VI, Vol. 3068, International Society for Optics and Photonics, 1997, pp. 182–193.
[44] Behrouz Safarinejadian, Navid Vafamand, Kalman randomized joint UKf algorithm for dual estimation of states and parameters in a nonlinear system, J. Electr. Eng. Technol. 10 (3) (2015) 1212–1220.
[45] Eleni N. Chatzi, Clemente Fuggini, Online correction of drift in structural identification using artificial white noise observations and an unscented Kalman filter, Smart Struct. Syst. 16 (2) (2015) 295–328.
[46] Steven Gillijns, Bart De Moor, Unbiased minimum-variance input and state estimation for linear discrete-time systems, Automatica 43 (1) (2007) 111–116.
[47] Steven Gillijns, Bart De Moor, Unbiased minimum-variance input and state estimation for linear discrete-time systems with direct feedthrough, Automatica 43 (5) (2007) 934–937.
[48] E Lourens, Costas Papadimitriou, Steven Gillijns, Edwin Reynders, Guido De Roeck, Geert Lombaert, Joint input-response estimation for structural systems based on reduced-order models and vibration data from a limited number of sensors, Mech. Syst. Signal Process. 29 (2012) 310–327.
[49] Konstantinos Tatsis, Vasilis Dertimanis, Imad Abdallah, Eleni Chatzi, A substructure approach for fatigue assessment on wind turbine support structures using output-only measurements, Procedia Eng. 199 (2017) 1044–1049.
[50] Nymfa Noppe, Konstantinos Tatsis, Eleni Chatzi, Christof Devriendt, Wout Weijtjens, Fatigue stress estimation of offshore wind turbine using a Kalman filter in combination with accelerometers, in: Proceedings of the ISMA, 2018, pp. 9.
[51] Sofia Puerto Tchemodanova, Masoud Sanayei, Babak Moaveni, Konstantinos Tatsis, Eleni Chatzi, Strain predictions at unmeasured locations of a substructure using sparse response-only vibration measurements, J. Civi. Struct. Health Monit. 11 (4) (2021) 1113–1136.

[52] Sergio Bittanti, Sergio M. Savaresi, On the parametrization and design of an extended Kalman filter frequency tracker, IEEE Trans. Automat. Control 45 (9) (2000) 1718–1724.
[53] Murali R. Rajamani, James B. Rawlings, Estimation of the disturbance structure from data using semidefinite programming and optimal weighting, Automatica 45 (1) (2009) 142–148.
[54] Ka-Veng Yuen, Ka-In Hoi, Kai-Meng Mok, Selection of noise parameters for Kalman filter, Earthq. Eng. Eng. Vib. 6 (1) (2007) 49–56.
[55] Per Christian Hansen, Dianne Prost O'Leary, The use of the L-curve in the regularization of discrete ill-posed problems, SIAM J. Sci. Comput. 14 (6) (1993) 1487–1503.
[56] Ulrika Lagerblad, Henrik Wentzel, Artem Kulachenko, Dynamic response identification based on state estimation and operational modal analysis, Mech. Syst. Signal Process. 129 (2019) 37–53.
[57] Raman Mehra, Approaches to adaptive filtering, IEEE Trans. Automat. Control 17 (5) (1972) 693–698.
[58] Charles G. Hilborn, Demetrios G. Lainiotis, Optimal estimation in the presence of unknown parameters, IEEE Trans. Syst. Sci. Cybern. 5 (1) (1969) 38–43.
[59] R. Kashyap, Maximum likelihood identification of stochastic linear systems, IEEE Trans. Automat. Control 15 (1) (1970) 25–34.
[60] Raman Mehra, On the identification of variances and adaptive Kalman filtering, IEEE Trans. Automat. Control 15 (2) (1970) 175–184.
[61] R. Mehra, On-line identification of linear dynamic systems with applications to Kalman filtering, IEEE Trans. Automat. Control 16 (1) (1971) 12–21.
[62] Brian J. Odelson, Murali R. Rajamani, James B. Rawlings, A new autocovariance least-squares method for estimating noise covariances, Automatica 42 (2) (2006) 303–308.
[63] Stefan Wernitz, Eleni Chatzi, Benedikt Hofmeister, Marlene Wolniak, Wanzhou Shen, Raimund Rolfes, On noise covariance estimation for Kalman filter-based damage localization, Mech. Syst. Signal Process. 170 (2022) 108808.
[64] S.C. Rutan, Adaptive Kalman filtering, Anal. Chem. 63 (22) (1991) 1103–1109.
[65] Roy R. Craig Jr., A review of time-domain and frequency-domain component mode synthesis method, 1985.
[66] Frank Naets, Jan Croes, Wim Desmet, An online coupled state/input/parameter estimation approach for structural dynamics, Comput. Methods Appl. Mech. Engrg. 283 (2015) 1167–1188.
[67] Imad Abdallah, Konstantinos Tatsis, Eleni Chatzi, Fatigue assessment of a wind turbine blade when output from multiple aero-elastic simulators are available, Procedia Eng. 199 (2017) 3170–3175.
[68] Charles Van Loan, Computing integrals involving the matrix exponential, IEEE Trans. Automat. Control 23 (3) (1978) 395–404.
[69] Tommaso Tamarozzi, Enrico Risaliti, Ward Rottiers, Wim Desmet, et al., Noise, ill-conditioning and sensor placement analysis for force estimation through virtual sensing, in: International Conference on Noise and Vibration Engineering (ISMA2016), KATHOLIEKE UNIV LEUVEN, DEPT WERKTUIGKUNDE, 2016, pp. 1741–1756.
[70] Silvia Vettori, Emilio Di Lorenzo, Bart Peeters, Eleni Chatzi, Kalman-based coupled response-input estimation during environmental tests on the box assembly with removable component structure, in: Proceedings of the 11th International Conference on Structural Dynamics, Athens, Greece, 2020, pp. 23–26.
[71] Konstantinos Tatsis, E. Lourens, A comparison of two Kalman-type filters for robust extrapolation of offshore wind turbine support structure response, in: Life-Cycle of Engineering Systems: Emphasis on Sustainable Civil Infrastructure: Proceedings of the Fifth International Symposium on Life-Cycle Civil Engineering (IALCCE 2016), 16-19 October 2016, CRC Press, Delft, the Netherlands, 2016, p. 209.
[72] Silvia Vettori, Emilio Di Lorenzo, Bart Peeters, Eleni Chatzi, A virtual sensing approach to operational modal analysis of wind turbine blades, in: Proceedings of ISMA2020 International Conference on Noise and Vibration Engineering, Leuven, Belgium, 2020.
[73] Marcin M. Luczak, Riccardo Riva, Süleyman C. Yeniceli, Steen Hjelm Madsen, Emilio Di Lorenzo, Identification of the test setup influence on the modal properties of a short wind turbine blade during fatigue test, Measurement 174 (2021) 108960.
[74] Roberta Cumbo, Lorenzo Mazzanti, Tommaso Tamarozzi, Pavel Jiranek, Wim Desmet, Frank Naets, Advanced optimal sensor placement for Kalman-based multiple-input estimation, Mech. Syst. Signal Process. 160 (2021) 107830.
[75] Lorenzo Mazzanti, Roberta Cumbo, Wim Desmet, Frank Naets, Tommaso Tamarozzi, An improved optimal sensor placement strategy for Kalman-based multiple-input estimation, in: Model Validation and Uncertainty Quantification, Volume 3, Springer, 2020, pp. 181–185.